The Dissertation Committee for Weinan Zhu Certifies that this is the approved version of the following dissertation:

Black Phosphorus Thin-film Transistors: From Strain Tunability to High Frequency Applications

Committee:

Deji Akinwande, Supervisor

Nanshu Lu

Jack Lee

Li Shi

Seth Bank

Black Phosphorus Thin-film Transistors: From Strain Tunability to High Frequency Applications

by

Weinan Zhu

Dissertation

Presented to the Faculty of the Graduate School of

The University of Texas at Austin

in Partial Fulfillment

of the Requirements

for the Degree of

Doctor of Philosophy

The University of Texas at Austin

August 2017

Dedication

To Kunzhi, my beloved hunsband, for the unconditional love and support.

To Kalico and Koala, for the joyful companion.

Acknowledgements

I am very fortunate that my past four years of Ph.D. study have prepared me ready for the next phase in life. First, I would like to thank my Ph.D. and thesis advisor, Dr. Deji Akinwande, for his strong guidance and support during the past four years, not only in my research but also in professional career development. I always feel grateful to have an advisor who would recommend *The Ph.D. Grind* in my first year of graduate school, who would choose both *Beethoven* and *Micheal Jackson* as the audio input during serious measurements, who would encourage me to step out of my comfort zone and teach me to stay positive when nothing seems to work out. I truly appreciate all the positive comments and constructive criticism that helped me through this Ph.D. exploration.

I have been very fortunate to join UT for my Ph.D. education where I have the chance to improve my intellectual development through either collaborating with and taking class from some of the best innovators. I would like to extend my thanks to Professors Nanshu Lu, Jung-fu Lin, Seth Bank, Keji Lai, and Li Shi, for their generous guidance and support in the collaborated projects. I am very grateful to Professors Jack Lee, Emanuel Tutuc and Steven Weinberg, and all my other teachers for essentially teaching me how to think critically and analytically as a young Ph.D. researcher.

Complex device research can be challenging, fortunately, the supportive atmosphere I experienced makes all these tedious lab works less stressful. I always enjoy working with my colleagues – Saungeun, Maruthi, Jason, Avinash, Sherry, Li, Rusty, and all my other group members. No fabrication of my devices is possible without the resources provided in UT and the support from MERTECH group. My special thanks to the recognition award back in my second year.

In the end, I would like to thank my beloved friends and family- Ting, my parents, my sis, and my husband, for their unconditional love and support behind each and every decision I have made, and to my two kittens, for their most precious companion while I was composing this final dissertation.

Black Phosphorus Thin-film Transistors: From Strain Tunability to High Frequency Applications

Weinan Zhu, Ph.D.

The University of Texas at Austin, 2017

Supervisor: Deji Akinwande

Flexible smart systems with functionalities of sensing and wireless communication have ignited worldwide interest. The main driving force behind this is the concept of Internet of Things (IoT), where the world is reshaped via digitalizing and connecting billions of smart devices. In this dissertation, we report on our research to advance the understanding and development of two-dimensional semiconductors for high performance robust flexible nano electronics and smart nano systems. Our interdisciplinary research approach involves nano characterizations, nano fabrication integrations, device physics, circuits, and thin-film mechanics. Specifically, this dissertation is composed with detailed discussion on following experimental works. In chapter 2, we discussed the ambient degradation of few layer black phosphorus (BP) and the development of effective dielectric encapsulation methodology for enhancing the air stability. In chapter 3, we presented the first few layer BP based flexible thin-film transistors and the circuit units realized from single and double BP TFTs. In addition, strong mechanical robustness was validated for the fully functional BP amplitude modulated AM demodulator. In chapter 4, we reported the first few layer BP flexible radio frequency (RF) transistor with cut-off frequency ~20 GHz, which successfully expanded the application scenario of 2D RF devices. In chapter

5, a polymer low-k dielectric based highly stretchable substrate was developed for investigating the strain tunabilities of 2D semiconductors. For few layer BP, thickness dependence in the angle-resolved Raman intensity evolvement under tensile strain was reported the first time.

Table of Contents

List of Tables

List of Figures

Chapter 1: Introduction

The rapid growth of the popularity of Internet-of-Things (IoT) in the past decade has resulted in strong urge of flexible electronics (Flextronics) with various functionalities ranging from sensing, computing to communicating. To fulfil the application scenario requirements, Flextronics with high speed and low power consumption as well as strong mechanical robustness are in need. Two-dimensional (2D) layered crystals are believed to be the natural candidates for flextronics applications, owing to their well-known features including the ultimate thickness scalability down to atomic thin, superior high intrinsic strain limit of ~20% and near ideal transparency.

Among the abundant 2D family, graphene from the elemental Xenes, MoS_2 from the compound MX_2/TMDs and insulating h-BN are most studied for the past decade.[1, 2] As the first experimentally obtained 2D layered crystal, monolayer graphene is believed to be promising for ultrahigh frequency applications owing to its superior fast carrier transport.[3-6] The unique Dirac cone band structure with zero band gap limits its current modulation therefore the applications in digital circuits, where on/off ratio is essential to provide sharp switch. Monolayer MoS_2 with sizable band gap of 1.9 eV, on the other hand, demonstrate high current on/off ratio reaching 10^7, makes it very promising for low power systems.[7-9] However, the naturally unipolar n-type transport and low carrier mobilities hinder its practical applications such as complementary inverters and high frequency RF circuits.[10-12] Since the year of 2014, few layer black phosphorus (BP) has been rediscovered as one of the most promising candidates in 2D family for its combined high carrier mobility ~1000 cm^2/Vs and thickness dependent direct band gap ranging from 0.3 eV to 2 eV. Its puckered honey comb lattice along armchair direction results in strong in-plane anisotropy in

mechanical, electrical and thermal properties, which make this novel material fascinating for fundamental studies such as strain tunabilities.[13, 14]

In chapter 2, we first introduced the crystal structure and basic electrical properties of few layer BP, where record high hole mobility ~1560 cm^2/Vs and high on/off ratio ~10^4 were obtained from a bottom gated device. The ambient degradation of BP was investigated via optical microscopy, atomic force microscopy (AFM), energy dispersive X-ray analysis (EDAX) and Raman spectroscopy. Conformal dielectric encapsulation method was developed to effectively enhance the air stability of BP transistors to months long.

In Chapter 3, the first realization of flexible BP transistors was presented with successful demonstration of circuit units including inverting and non-inverting amplifiers, ambipolar inverter, and frequency doubler. The fully functioning amplitude modulation (AM) demodulator based on single flexible BP transistor was demonstrated with detailed analysis on the square law demodulator behavior. The mechanical robustness of such flexible BP transistor as well as AM demodulator was investigated under tensile strain loading up to 2% and three-point bending up to 5000 cycles.

In chapter 4, the first flexible BP radio frequency (RF) transistor with top gated structure was presented with high intrinsic cut-off frequency f_T~17.5 GHz and f_{MAX}~14.5 GHz obtained. The mechanical robustness was also studied for the top gated RF transistors with extrinsic cut-off frequency and maximum oscillation frequency investigated under uniaxial strain up to 1.5%.

In Chapter 5, strain tunabilities on 2D layered semiconductors were studied with emphasis on the material characterizations. The uniaxial tensile strain was applied via a stretching platform, which is compatible with general 2D layered crystals, such as few layer BP and CVD MoS_2. Here in this work, results on phonon vibrational modes (Raman

detectable) and optical band gap dependence on tensile strain of beyond 2% in CVD MoS_2 were presented. Then, anisotropic response of angle-resolved Raman intensity of few layer BP under uniaxial strain were discussed in this work, with a strong thickness dependence observed.

Chapter 2: Air-Stable Multilayer Phosphorene Transistors

INTRODUCTION TO BLACK PHOSPHORUS

Despite the fact that this novel 2D layered semiconductor was rediscovered in the year of 2014, few layer black phosphorus and its monolayer counterpart phosphorene have gained worldwide attention for being one of the most promising 2D semiconductors with superior properties including high carrier mobility ~1000 cm^2/Vs, sizable current modulation ratios ~10^5, thickness dependent direct band gap ranging from 0.3 eV (bulk) to 2 eV (monolayer).[14, 15] Therefore, this material is believed to be most promising candidate in 2D semiconductors for high speed and power efficient nano electronics. The thickness tunable band gap also makes it a promising candidate for photonics, especially for near and mid-IR applications.

The crystal structure of few layer BP is shown in Figure 2.1 A. Each P atom forms three covalent bonds with its nearest neighbor P atoms in sp3 hybridizations,[16] and the puckered structure results in strong in-plane anisotropy along arm-chair (AC) and zig-zag (ZZ) orientations with respect to electrical, mechanical and thermal properties.[17, 18] The two anisotropic directions are identified in Figure 2.1 (A) and (B). Electron transport favors the AC direction for the relatively smaller effective mass; in the meantime, ZZ direction exhibit a higher thermal conductively. This orthogonal between high electron transport and thermal transport makes BP a promising candidate for thermal electronics with strong in-plane selectivity. Due to the this unique in-plane anisotropic property, an efficient methodology of determining the in-plane orientation of BP samples becomes rather critical in most practical applications. Here in this work, polarized Raman spectroscopy is used to effectively determine the crystal orientations due to the distinguished intensity ratios among the three characteristics peaks, A_g^1, B_{2g} and A_g^2, as shown in Figure 2.1 (C). [16, 19,

[20]A representative Tauc plot[21] generated from FTIR measurement is shown in Figure 2.1 (D) demonstrating the bulk range band gap of ~0.3 eV.

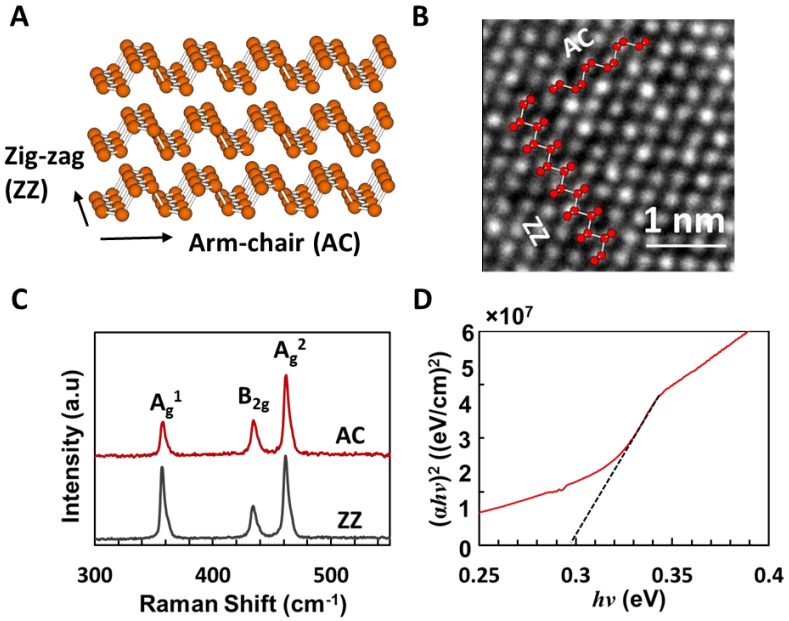

Figure 2.1: Crystal structure and material characterization of few layer BP. (A) Schematic of few layer BP with Zig-zag (zz) and Arm-chair (AC) edges identified. (B) High resolution TEM image of few layer BP. (C) Raman spectroscopy of few layer BP along both ZZ and AC directions. (D) A representative Tauc plot for estimating the optical bandgap of BP, which confirms a gap of ~0.3 eV in the bulk limit.

FABRICATION AND CHARACTERIZATION OF BP DEVICES

Global bottom gated structure was first adopted for investigating the electrical properties of few layer BP, therefore, highly P type doped Si with 25nm Al_2O_3 doposited via atomic layer deposition (ALD) was chosen as the substrate. Thin film of BP was obtained through mechanical cleavage from the bulk BP crystal, a general adopted method for obtaining atomically thin 2D layered crystals. After few layer BP flakes were exfoliated onto the substrate, 50nm Ti/Au source and drain contact stacks were formed using e-beam lithography and e-beam evaporation. Device schematic is shown in Figure 2.2 (B). Record

high hole carrier mobility ~1560 cm^2/Vs was achieved from a typical BG device with BP thickness ~15nm. As shown in Figure 2.2 (C), high on/off ratio was observed from the same device, which indicated the potential for this new 2D material for future high speed and low power nano electronics.

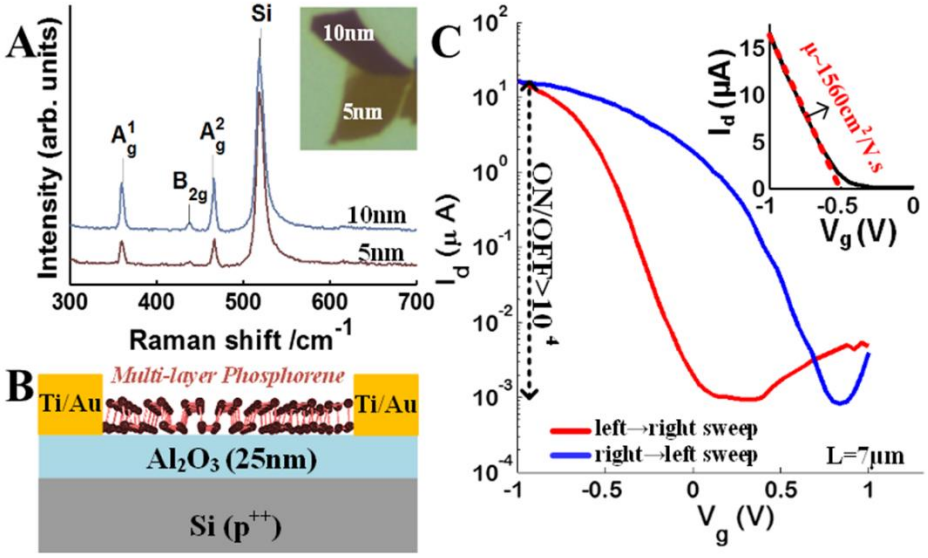

Figure 2.2: Few layer BP field effect transistors. (A) Raman spectrum of exfoliated BP fakes of 5nm and 10nm along zig-zag directions. Insert is the optical image of the exfoliated BP flakes. (B) Schematic of the bottom gated BP transistor. (C) Transfer characteristics of the device showing highest hole mobility reaching 1560 cm^2/Vs and current modulation of 10^4. Insert is the linear carrier mobility extraction.

BP Ambient Stability Issue and Dielectric Encapsulation

Despite the fascinating electrical performance obtained from the above work, the intrinsic hygroscopic nature of BP brings about severe challenges to its practical applications.[22-24] As shown in Figure 2.3, exfoliated few layer BP flake suffered from severer degradations with Solid-Bubble-Vapor (SBV) morphology change observed in both optical microscopy image and atomic force microscopic (AFM) images while stored

in ambient environment. The hygroscopic nature induced surface SBV degradation started within 1 hour after exfoliation as shown in the 3D AFM image, therefore, minimizing the exposure time of BP surface to ambient environment and seeking effective long-term encapsulation are in great necessity for enhancing the air stability of BP based nano electronics.

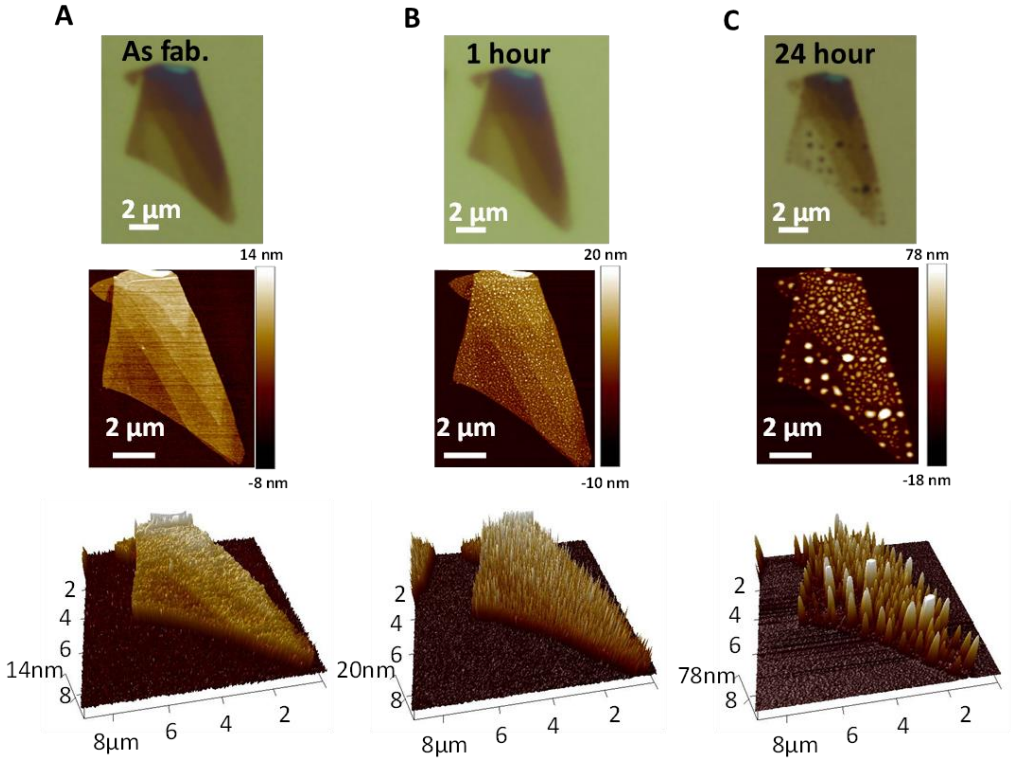

Figure 2.3: Ambient stability issue of hygroscopic BP.

Compositional analysis of fully degraded phosphorene was performed by energy dispersive X-ray analysis (EDAX) in the scanning electron microscopy (SEM) chamber. The phosphorene sample in Fig. 2.4 was exfoliated onto an Au/Si substrate and kept in air for three days. Before SEM-EDAX analysis, the sample was baked on a hot plate at 100 °C for 10 minutes. From the AFM data, the two droplet-like spots on the phosphorene

surface show a height of 78 nm, much taller than nearby flat regions. The EDAX maps reveal significant oxygen signals on the degraded flake, indicative of oxidation in the aging process.

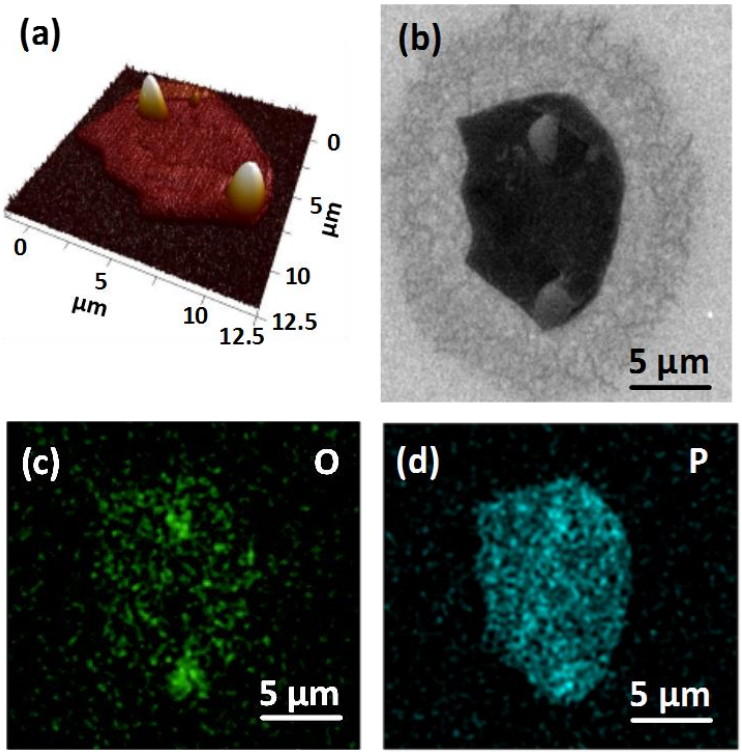

Figure 2.4: (a) 3D AFM image and (b) SEM image of a degraded phosphorene sample. (c) and (d) EDAX maps of oxygen and phosphorus signal in the same sample. The clear oxygen signals indicate certain oxidation process that contributes to the degradation of black phosphorus.

High-k dielectric Al_2O_3 was deposited onto BP flakes as thin encapsulation layer, as shown in Figure 2.5 (a). Thin layer of Al_2O_3 with thickness approximating 5nm was first invested with microwave impedance microscope (MIM) measurements,[25] where both

morphology and conductivity information were obtained simultaneously at AFM resolutions. The same capped BP flake was measured for one week to track the degradation process. As shown in Figure 2.5 (b), with thin layer dielectric encapsulation, there was no obvious degradation observed in the morphology/AFM height profile. However, the measured sheet resistance increased sharply by two orders indicating strong electronic degradations. For longer exposure time in the ambient, the highly conductive regions propagated toward the center of the flake. This edge initiated degradation was also verified by Raman spectroscopy mapping data, shown in Figure 2.5 (d).

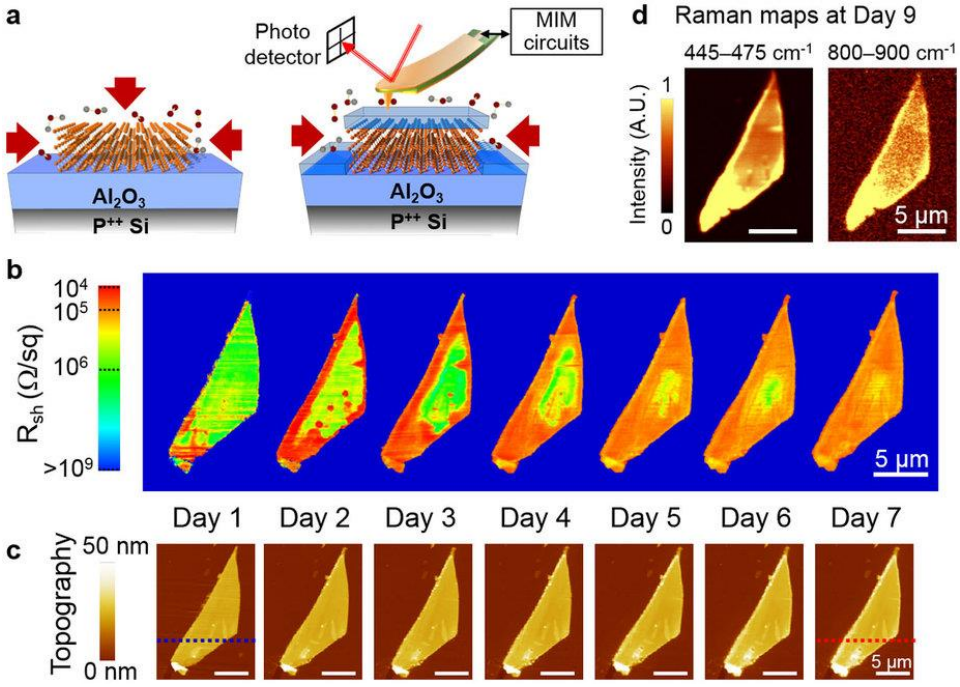

Figure 2.5: Spatial and temporal evolution of few layer phosphorene with thin dielectric encapsulation.[23]

Interestingly, a relatively small and broad bump likely composed of several new Raman modes can be seen in the spectrum in Fig. 2.6 at higher wavenumbers (800–900

cm^{-1}) which confined to the BP flake. Compared with published literatures,[22, 26] this new Raman bump is consistent with the vibrations of mixed phosphorus oxide compounds.

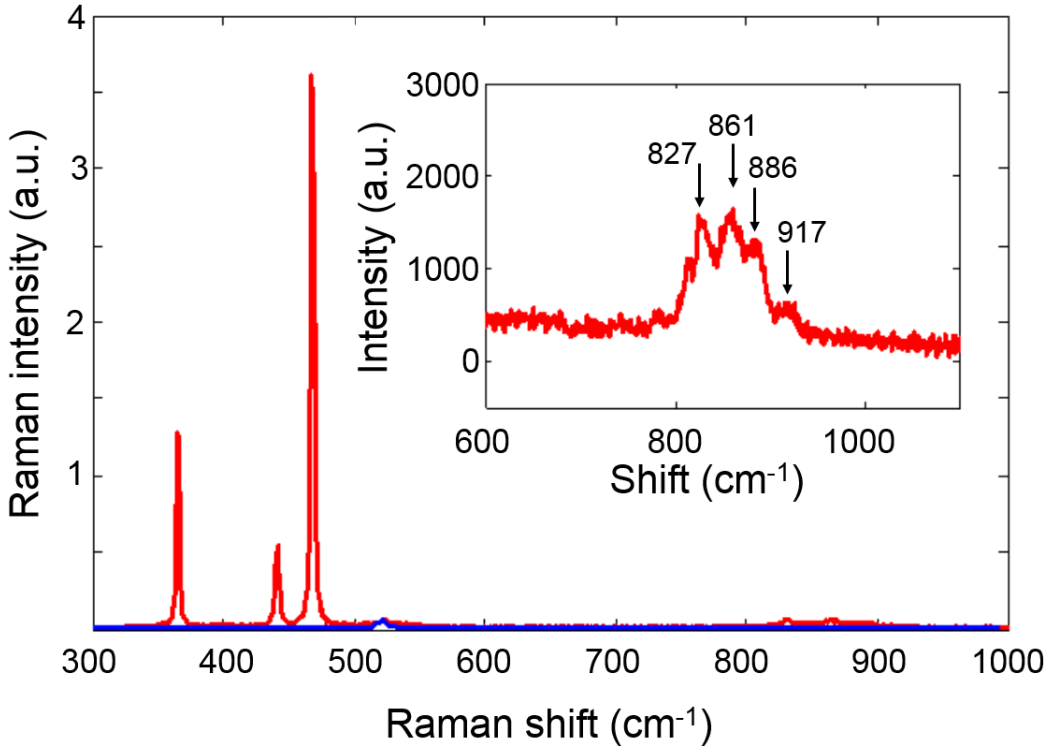

Figure 2.6: Raman spectra of a typical degraded phosphorene flake (red line) and the Al_2O_3/P^{++} Si background (blue). The inset shows the detailed Raman spectrum of the degraded phosphorene with several peaks from 800 to 950 cm^{-1}. These Raman signatures are consistent with the reported P-O stretching modes due to oxygen-containing black phosphorus compounds.

As seen from both the MIM and Raman data, the edge initiated degradation process suggest that a capping layer thinner than the flake may offer poor sidewall coverage, hence relatively ineffective against moisture adsorption at the edges. Therefore, 25nm thick ALD Al_2O_3 was adopted as conformal capping layer with fully covered sidewalls to provide sufficient encapsulation of few layer BP for nano electronics. Long term air stability was achieved while using 25nm Al_2O_3/DuPont Teflon-AF stack as encapsulation layer, as

shown in Figure 2.7, where both on-state current and on/off ratio were well preserved after 79 days exposure in ambient environment.[23]

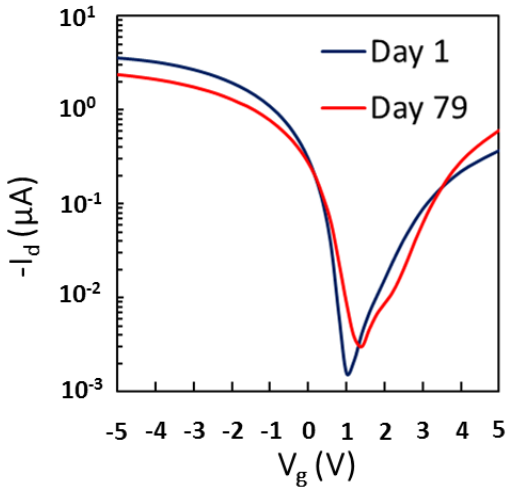

Figure 2.7: Transfer characteristics of few layer BP transistor showing long term ambient stability enhanced by dielectric encapsulation.

CONCLUSION

Here in this chapter, we discussed the crystal structure of bulk and few layer BP with emphasis on its strong in-plane anisotropy in electrical, thermal and mechanical properties induced by the buckle structure. With successful demonstration of few layer BP transistors on Al_2O_3/Si substrate, we validated the promising electrical performance of few layer BP with high carrier mobility ~1000 cm^2/Vs and high current modulation ~10^4 obtained simultaneously. This performance achieved in BP transistors cannot be well preserved in ambient environment due to its hygroscopic nature, which leads to quick oxidation of the channel material and to severe degradation of the device performance. We investigated the mechanism of this SBV degradation of BP by long term OM and AFM observations. SEM-EDAX and Raman spectroscopy analysis were conducted in this work

to further validate this oxidation induced degradation of BP. To preserve the superior electrical performance of BP even after long term ambient exposure, an effective dielectric encapsulation method was developed, where conformal coverage of BP formed by 25nm Al_2O_3/DuPont Teflon-AF stack effectively protected the channel BP from oxidation. With this dielectric encapsulation, BP transistor with high carrier mobility and high on/off ratio can be well preserved after 79 days of exposure in ambient environment. This paves the way towards air-stable BP thin-film transistors for flexible electronics devices and circuits applications.

Chapter 3: Flexible Black Phosphorus Ambipolar Transistors and Circuits

(Reproduced with permission from W. Zhu, Y. Yogeesh, S. H. Aldave, J.S. Kim, S. Sonde, L. Tao, N. Lu and D. Akinwande, "Black Phosphorus Ambipolar Transistors, Circuits and AM Demodulator", *Nano Lett,* vol. 15, pp. 1883-90, Mar 11 2015)

Weinan Zhu[†], Maruthi N. Yogeesh[†], Shixuan Yang[‡], Sandra H. Aldave[†§], Joon-Seok Kim[†], Sushant Sonde[†], Li Tao[†], Nanshu Lu[‡], and Deji Akinwande[†]*

†Microelectronics Research Center, Department of Electrical and Computer Engineering, The University of Texas at Austin, Austin, TX, 78758, USA.

‡Department of Aerospace Engineering and Engineering Mechanics and Texas Materials Institute, The University of Texas at Austin, Austin, TX, 78712, USA.

§ Polymer Science and Technology Department, University of the Basque Country, San Sebastian, Guipuzcoa, 20018, Spain.

ABSTRACT

High-mobility two-dimensional (2D) semiconductors are desirable for high-performance mechanically flexible nanoelectronics. In this work, we report the first flexible black phosphorus (BP) field-effect transistors (FETs) with electron and hole mobilities superior to what has been previously achieved with other more studied flexible layered semiconducting transistors such as MoS_2 and WSe_2. Encapsulated bottom-gated BP ambipolar FETs on flexible polyimide afforded maximum carrier mobility of about

310cm^2/V·s with field-effect current modulation exceeding three orders of magnitude. The device ambipolar functionality and high-mobility were employed to realize essential circuits of electronic systems for flexible technology including ambipolar digital inverter, frequency doubler, and analog amplifiers featuring voltage gain higher than other reported layered semiconductor flexible amplifiers. In addition, we demonstrate the first flexible BP amplitude-modulated (AM) demodulator, an active stage useful for radio receivers, based on a single ambipolar BP transistor, which results in audible signals when connected to a loudspeaker or earphone. Moreover, the BP transistors feature mechanical robustness up to 2% uniaxial tensile strain and up to 5000 bending cycles.

INTRODUCTION

Two-dimensional (2D) crystalline nanomaterials have generated widely growing interest for diverse applications on mechanically soft flexible substrates owing to their generally inert surface, high elasticity, and thickness scalability down to a monolayer, which represents the ideal limit for electrostatic control, optical transparency, and bendability.[8, 15, 27-34] Over the last decade, graphene has been the foremost 2D atomic crystal investigated for flexible nanoelectronics with substantial advances in large-scale synthesis, device mobility, cutoff frequency, strain tolerance and mechanical robustness.[28-31, 35-37] However, its lack of a bandgap results in a transistor that cannot be switched off by a gate voltage, an indispensable requirement for the vast majority of circuits in modern electronic systems.[28] Recently, transitional metal dichalcogenides (TMDs) such as MoS_2 and WSe_2 have emerged as suitable layered semiconductors that offer a sizeable bandgap attractive for low-power electronics.[7, 8, 32, 33, 38] Nonetheless, despite promising theoretical prospects,[9, 39] experimental TMD device mobilities have been relatively low, less than 50 cm^2/V·s on flexible substrates so far,[32, 40-43] a value comparable to established amorphous

materials such as metal oxide semiconductors that have transitioned into application products.[44-46]

To achieve higher carrier mobilities while retaining suitable field-effect current modulation, we have investigated black phosphorus (BP) devices on flexible substrates for the first time. Black phosphorus, otherwise known as phosphorene in the thin-film limit,[15, 34] is a layered semiconducting 2D crystal similar to graphene but with a physically distinct puckered structure.[19, 47] It is experiencing rapidly increasing research activity for a myriad of optoelectronic devices,[48-52] owing to its i) high experimental mobility up to ~1000cm^2/V·s,[15] and ii) thickness dependent direct bandgap spanning the infrared to visible regimes.[53]

In this work, flexible BP devices are realized on polyimide substrates affording maximum device mobility of ~310cm^2/V·s, more than five times larger than the highest mobility achieved with flexible TMD transistors.[32, 40-43] Ambipolar field-effect current modulation exceeds 10^3 with sustained device performance at 2% uniaxial strain and after 5000 bending cycles that is ultimately limited by the mechanical robustness of the gate dielectric.[32] Based on the ambipolar functionality and high mobility, we demonstrate several circuit blocks essential for future flexible nanoelectronic systems, including ambipolar inverter, frequency doubler, and inverting and non-inverting analog amplifiers with voltage gains of ~8.7, more than two times higher than previous flexible thin-film amplifiers.[38, 54, 55] Lastly, a flexible amplitude-modulated (AM) demodulator was developed based on a single BP ambipolar transistor that yielded audible signals when connected to a loudspeaker or earphone. Our results indicate that black phosphorus is the most promising layered semiconductor for flexible nanoelectronics.

BP Preparation and Device Fabrication

The crystalline nature of multi-layer black phosphorus investigated in this work was verified with both high-resolution transmission electron microscopy (HRTEM) and Raman spectroscopy. Fig. 3.1(a) displays the HRTEM top-view image of a typical multi-layer BP flake highlighting both the arm-chair (AC) and zig-zag (ZZ) edges. Raman spectroscopy of several mechanically exfoliated samples (Fig. 3.1(b)) with thickness between 5nm and 15nm revealed the three characteristic vibrational modes (A_g^1, B_{2g} and A_g^2) of black phosphorus further confirming the chemical identity of the thin films. Owing to the puckered anisotropic crystal structure of black phosphorus, Raman intensity ratios among the three peaks are highly sensitive to its in-plane crystal orientation.[14, 16] This light-matter orientation dependence can be routinely used to determine the orientation of BP flakes with respect to the charge transport direction in fabricated transistor devices. The Raman spectra featured in Fig. 3.1(b) represents the AC direction for flakes with thickness of 5nm, 10nm, and 15nm, and the ZZ direction for the 13nm flake profiled in the insert of Fig. 3.1(c). To achieve high-speed charge transport in BP transistors, it is known that the AC direction affords lower effective mass and correspondingly higher mobilities compared to other crystal orientations.[18, 47] In this work, all Raman spectra were measured after device fabrication and electrical measurements were completed to avoid potential damage to the BP flakes from the Raman laser.

To fabricate the transistor devices, few-layer semiconducting black phosphorus was first mechanically exfoliated from commercial supplies (from Smart-elements) onto polyimide (PI) substrate as channel material for bottom gate field-effect transistors (FETs). Due to the lack of established synthesis method for either monolayer or multi-layer black phosphorus, exfoliation was employed as an effective route for obtaining BP flakes (thickness $\leq$ 15nm) with micro-meter lateral dimensions. Fig. 3.1(c) displays the optical

image and atomic force microscopy (AFM) thickness measurement of a typical exfoliated BP flake with a smooth and uniform surface, necessary features for nanoelectronic devices. An optical image of a flexible PI substrate with encapsulated BP electronic devices is shown in Fig. 3.1(d) with inherent flexibility and stability for ambient operation.

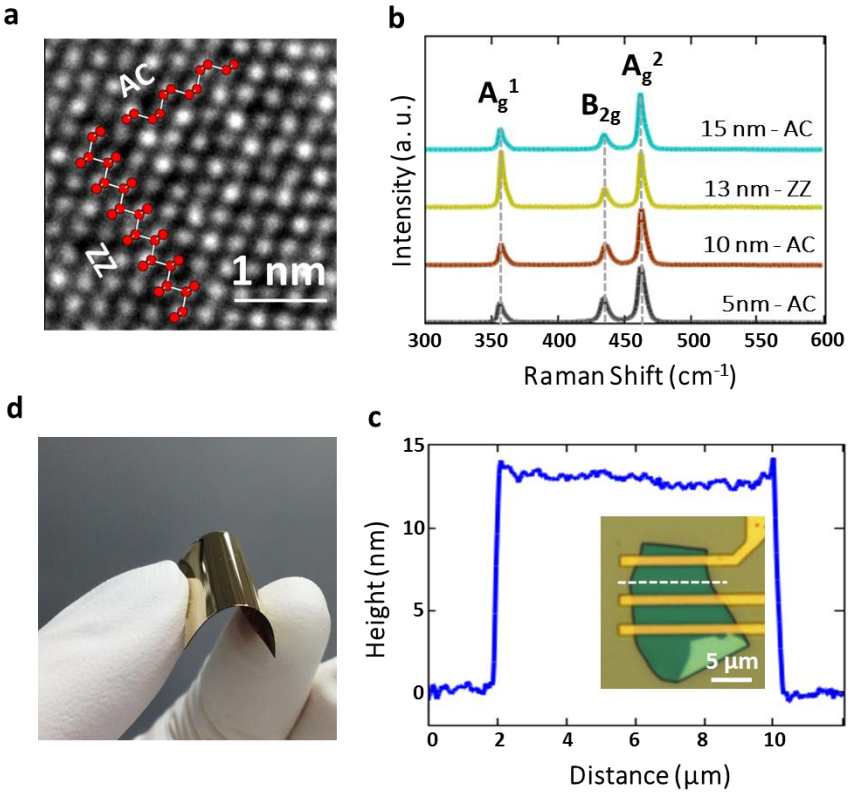

Figure 3.1: TEM, Raman, Optical and AFM characterization. (a) HRTEM of few-layer black phosphorus. AC and ZZ edges are identified accordingly. (b) Raman spectroscopy of typical BP flakes explored in this work with thickness of 5nm, 10nm, 13nm and 15nm. 532nm linearly polarized laser was employed. The black phosphorus characteristic peaks, A_g^1, A_g^2, and B_{2g}, are clearly resolved, and the intensity ratio among the three peaks indicate that the in-plane laser polarization is along either the armchair (AC) or zigzag (ZZ) directions. (c) AFM height profile of a BP flake with measured AFM thickness of 13nm corresponding to the dashed line in the insert, which is the optical image of the bottom-gate transistors based on this flake. (d) Optical image of few-layer BP devices on a flexible substrate.

DC PERFORMANCE OF FLEXIBLE BP TRANSISTOR

The transistor device structure on flexible polyimide developed in this work is illustrated in Fig. 3.2(a), featuring an embedded bottom-gate for field-effect,[29, 32] and black phosphorus encapsulation for air-stability.[56, 57] Commercial PI (Kapton) was utilized as the flexible substrate followed by double-sided spin-coated cured liquid PI to achieve nanoscale smooth surfaces with roughness of ~1-3nm.[58] The global bottom-gate was realized by electron beam evaporation of Ti/Pd metal stack with 3nm/50nm thickness. 25nm Al_2O_3 deposited by atomic layer deposition (ALD) was used as bottom gate dielectric, which yields a measured gate oxide capacitance of 0.21μF/cm^2 and affords routine visual identification of suitable BP flakes by optical microscopy. BP flakes were exfoliated onto the substrate and immediately covered with polymethyl methacrylate (PMMA), an electron beam resist to prevent air-degradation of black phosphorus during device fabrication. Accurate flake thickness was determined by AFM after completion of electrical measurement experiments. Source and drain contacts were formed by electron beam lithography and deposition of 1.5nm/70nm Ti/Au metal stack, which was selected due to its high work function and reduced injection barrier to the valence band.[59-61] Afterwards, another layer of 25nm Al_2O_3 was deposited by ALD to encapsulate the BP devices, which proved effective in maintaining stable electrical properties over the weeks-long duration of experiments under ambient conditions (Fig. 3.3).

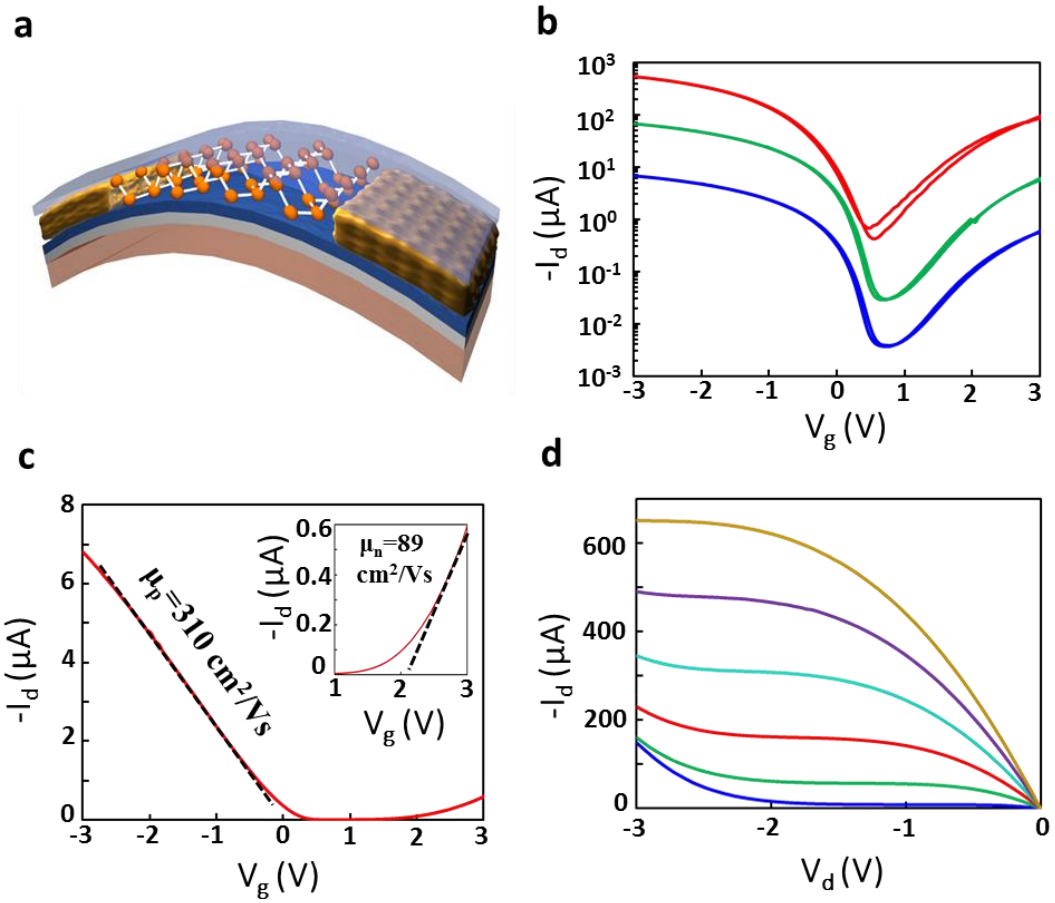

Figure 3.2: Schematic and current-voltage characteristics of bottom-gate (BG) BP FETs on flexible substrate. (a) Simplified illustration of the device structure of flexible BG BP FET on PI substrate (not to scale). Ti/Pd/Al_2O_3 with 3nm/50nm/25nm thickness was deposited as global bottom gate and gate dielectric stack. Ti/Au with 1.5nm/70nm thickness is lithographically formed as the metal contacts to the semiconducting BP channel. A top-side layer of 25nm Al_2O_3 was deposited for device encapsulation. (b) Log plot of the transfer characteristics of encapsulated BG BP FET on PI, showing $>10^3$ on/off ratio, negligible hysteresis, and clear ambipolar character. Drain bias is V_d=-10mV, -100mV and -1V from bottom to top. Flake thickness is 15nm, and W/L=10.6μm/2.7μm. (c) Linear plot of transfer characteristics at V_d=-10mV, showing low-field hole μ_h of 310 cm^2/Vs. Electron mobility (μ_e) was extracted to be 89 cm^2/Vs for this device, as is shown in the insert. (d) Output curves of the same device displaying current saturation. Gate bias, V_g = 0 to -2.5 V from bottom to top, with a step size of -0.5 V.

Outstanding device performance including high mobility, strong current saturation, and ambipolar transport were observed at room temperature in ambient environment for the encapsulated flexible BP transistors. The transport direction aligned well with the AC crystal orientation based on the Raman spectrum (Fig. 3.1(c)) taken after the device fabrication. Transfer characteristics with negligible hysteresis were achieved (Fig. 3.2(b)) owing to the effective ALD encapsulation and protection against moisture adsorption.[56, 57] Drain current modulation approaching four orders of magnitude was obtained on BP device with film thickness of 15nm, which is much higher than recently reported values of about ten.[14, 34] We attribute this improvement to the Al_2O_3 encapsulation layer that effectively reduces the residual charge adsorbed from the ambient environment at the black phosphorus surface, thereby affording greater gate control in switching the device. With negligible electrical hysteresis, charge transport can be accurately analyzed. The extracted low-field hole mobility (μ_h) using the Y-function linear slope method[62] was 310cm^2/Vs, which is much higher than state-of-the-art semiconducting TMD, organic and metal oxide flexible transistors.[32, 40-43] Long term air stability was obtained owing to the effective dielectric encapsulation. As shown in Fig. 3.3, lonely slight shift in the minimum conduction point and reduction of on state current was observed after 17 days of fabrication. There is no significant increase of hysteresis observed, which indicated well preserved channel against ambient degradation.

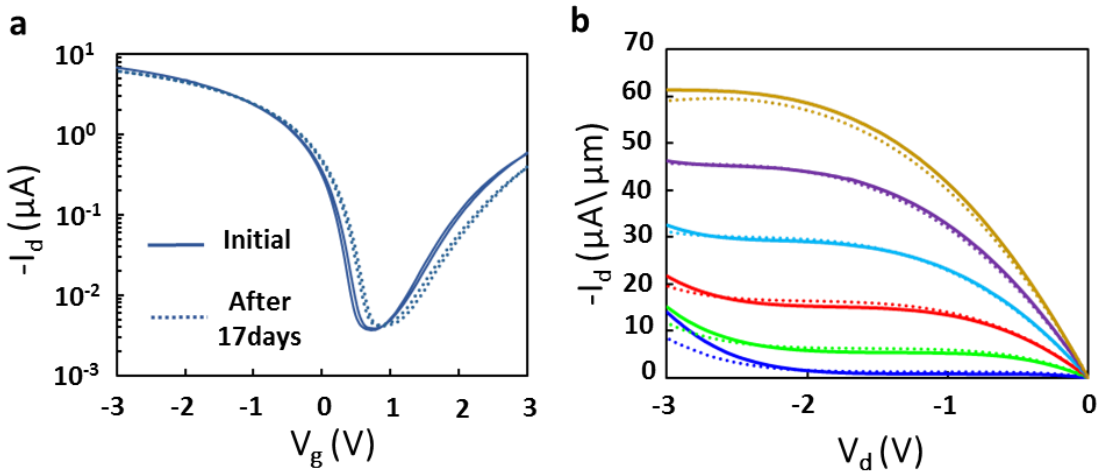

Figure 3.3: Long term stability of flexible BP transistors. (a) Transfer characteristics of an encapsulated device at initial measurement after device characterization (solid line) and after 17 days (dash line). Drain bias V_d=-10mV. Both forward and backward V_g sweep are presented, showing negligible hysteresis. Overall performance regarding I_{on}, drain current modulation, and hysteresis in V_g were well preserved, with only slight shift of 0.12V in the minimum conduction point. (b) Output characteristics of the same device, measured under the same conditions (initial data – solid line, after 17 days – dash line). On state current was well preserved with negligible current fluctuation. Gate bias varied from V_g=0V to -2.5V with a step size of -0.5V from the bottom to the top curve. Geometry for this transistor device is W/L=10.6μm/2.7μm, with flake thickness of 15nm as determined by atomic force microscopy.

A comparison of our flexible BP and the highest reported flexible thin-film semiconductor transistors with respect to carrier mobility and current modulation are listed in Table 3.1. In addition to the high hole mobility that is superior to that of semiconducting p-type TMDs, ambipolar black phosphorus can afford field-effect electron mobility (μ_e) exceeding that of n-type TMDs as shown in Table 3.1, where the electron mobility of BP FET (~89cm^2/Vs) is ~3 times higher than the highest reported value for contemporary MoS_2 flexible transistors.[32] This μ_e is also the highest number reported for BP transistors so far, despite the fact that the present BP devices are not optimized for electron transport,

indicating overall n-type device improvement can be expected with contacts that preferentially favor electron transport.[60, 61, 63] In addition, strong saturation was achieved in the output characteristics (Fig. 3.2(d)), a necessary feature for realizing high cutoff frequencies for power gain, and high-performance analog amplifiers and circuits.[28, 29]

To further investigated the thickness dependence of flexible BP thin film transistor performance in terms of low field carrier mobility and drain current modulation, statistics of more than 20 BP transistors were created. As shown in Fig. 4, thinner sample tend to have higher current on/off ratio while the relatively thicker sample exhibit higher mobility. For BP sample with thickness within 5~15 nm, the average mobility ~100-200 cm^2/Vs while the on/off ratio is ~10^3-10^4.

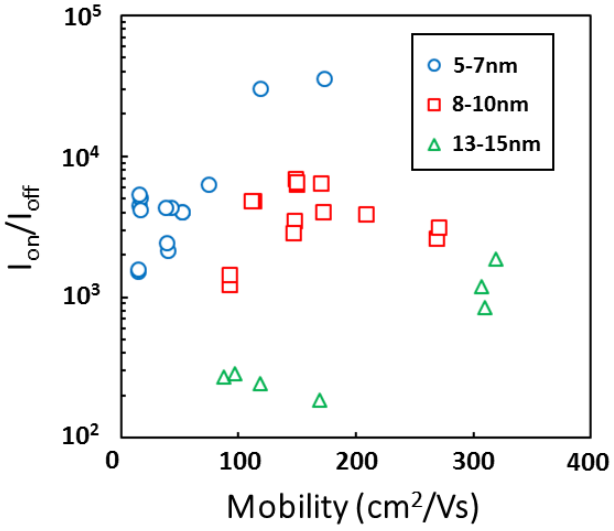

Figure 3.4: Statistics of hole carrier mobility and drain current modulation of unstrained flexible BP transistors studied in this work. Data are grouped according to the thickness of BP channel. Besides the highest mobility, ~310 cm^2/Vs (15nm), and highest on/off ratio, ~3×10^4 (5nm), 65% of devices afford mobility >100cm^2/Vs and 85% of devices exhibited current on/off ratio >10^3. All mobilities were extracted using linear Y-function method from transfer curves with drain bias of -10mV, and data for both forward and backward sweep are included in this figure separately.

Material	FET mobility ($cm^2/V \cdot s$)		ON/OFF ratio	Film thickness (nm)	Transport Type
	μ_e	μ_h			
Black phosphorus (this work)	89	310	10^3-10^4	15	ambipolar
	3	180	10^4-10^5	5	ambipolar
MoS_2 ref [32]	30	-	10^7-10^8	10	n-type
WSe_2 ref [40]	24	45	10^7	1.5	ambipolar
SnS_xSe_{2-x} ref [41]	12	-	10^6	5	n-type
Pentacene ref [42] _ENREF_20	-	8.85	10^3-10^4	65	p-type
InGaZnO ref[43]	76	-	10^5	23	n-type

Table 3.1: Basic comparison of flexible thin-film semiconducting transistors including black phosphorus (this work), layered metal dichalcogenides, organic semiconductor and metal oxide semiconductors. The table features the state-of-the-art device metrics for each thin-film material. Data is for μm-sized devices at room temperature.

FLEXIBLE BP AMBIPOLAR CIRCUITS

The attractive device metrics of high mobilities, strong current saturation, direct bandgap and sizeable on/off ratio motivates the interest in black phosphorus for both high-speed digital and analog thin-film transistors and circuits on flexible substrates. Circuits that can provide essential functions including ambipolar inverter, frequency doubler and demodulator, and inverting and non-inverting voltage amplifiers were successfully realized based on single/double BP transistors. The capability to realize functional circuits based on a small count of BP transistors is particularly attractive for the nascent flexible nanoelectronics applications where large-scale integration has not yet been developed unlike modern semiconductor technology.

Flexible BP Ambipolar Inverter

The inverter device structure enabled by the ambipolar transport characteristics in fabricated BP FETs as well as the high drain current modulation, was successfully achieved by splitting the minimum conduction points of two series transistors, similar in concept to graphene ambipolar inverters.[64] For ambipolar inverters, a relatively thicker BP flake (t=15nm) was chosen for its favorable lower bandgap of ~0.3eV,[34, 53] a small value that typically leads to ambipolar transport characteristic due to the relatively lower Schottky barrier height for the minority carrier (electron) injection compared to thinner films that will present a larger Schottky barrier and reduced ambipolarity.[60, 61] Two identical bottom gate transistors fabricated from the 15nm-thin flake were combined into a complementary inverter circuit, with the global bottom gate as the input, and the center terminal as the output (Fig. 3.6 insert). The inverting functionality is shown in Fig. 3.5, where peak inverting gain is ~4.5.

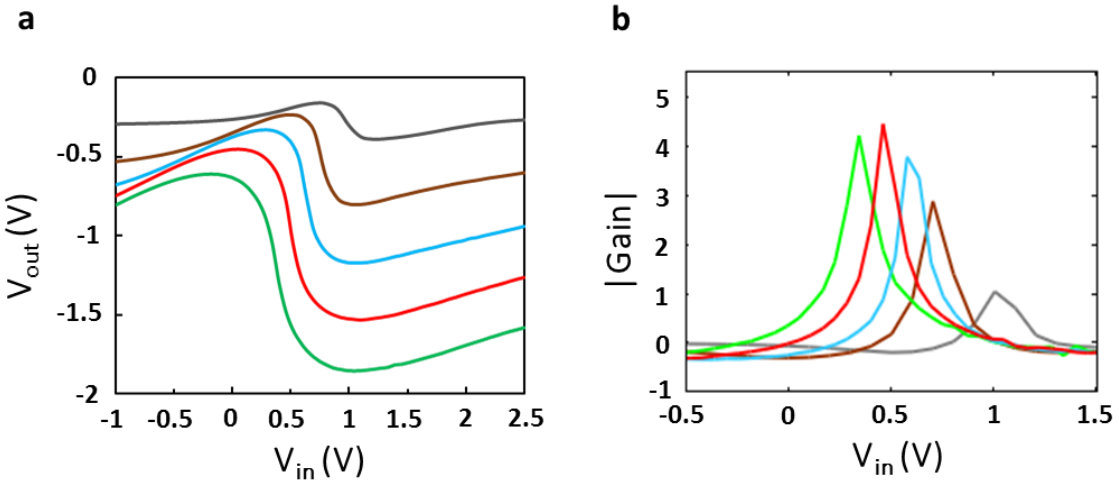

Figure 3.5: Inverter output pulse showing a gain of ~1.6. Flexible BP ambipolar inverter functionality and inverter gain. (a) Inverter functionality of flexible BP ambipolar inverter was observed with the input V_g bias swept from -1V to 2.5V, and V_{dd} increased from -0.5V to -2.5V with a step size of -0.5V, from the top curve to the bottom curve. Large output voltage swing (>1V) was observed for V_{dd}=-2V (red curve). (b) Corresponding inverter gain. The peak inverter gain $|V_{out}/V_{in}|$ was 4.6 at V_{dd}=-2V and V_g=0.46V.

Based on the ambipolar inverter, a push-pull amplifier, which is a fundamental circuit for output voltage stages,[65] was realized as shown in Fig. 3.6. An input pulse signal with peak-to-peak amplitude (V_{pp}) of 0.5V was connected to the gate input, and the amplified inverted signal was observed at the center output terminal with an output/input voltage gain of ~1.68 (Fig. 3.6). The push-pull amplifier operates at a maximum frequency of 100Hz, which is limited by the very large parasitic capacitance from the bottom gate structure. By optimizing the device structure, e.g., utilizing isolated top gate or patterned bottom gate electrodes,[29, 66] higher frequency operation will be accessible.[38, 67] Previously, we showed in Ref. 4 that patterned embedded-gate graphene flexible transistor with 0.5μm channel length afforded intrinsic cutoff frequency of 25GHz. By replacing the graphene channel material with black phosphorus, we estimate that similar optimized 0.5μm BP flexible transistor could yield cutoff frequency exceeding 1GHz based on the experimental mobility of 310$cm^2/V{\cdot}s$ achieved in this work. Moreover, Wang et al. has recently reported 20GHz cutoff frequency for 0.3μm BP FET on hard substrate,[66] further highlighting the high frequency prospects of this nanomaterial.

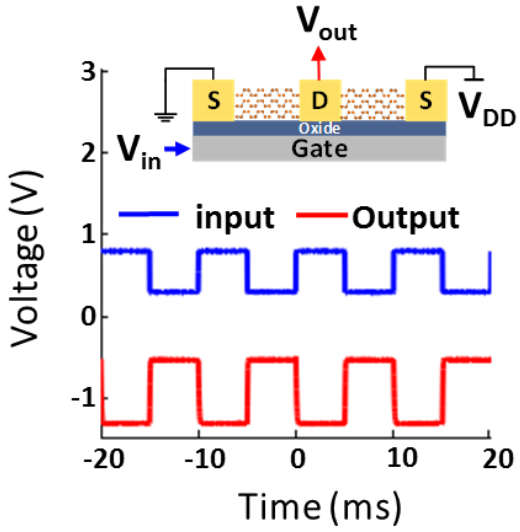

Figure 3.6: Ambipolar digital inverter. DC bias V_g=-0.46V and V_{dd}=-2V. Input pulse oscillates at 100Hz with peak-to-peak amplitude (V_{pp}) of 0.5V. Inverter output pulse showing a gain of ~1.6.

Flexible BP Amplifier

Inverting and non-inverting single-transistor amplifiers (Fig. 3.3(b) and (c)) are among the most important circuit units for analog signal processing and require both current saturation in the device output characteristics and high transconductance (g_m) to achieve high voltage gain.[28, 32] In this work, both inverting (i.e. common-source) and non-inverting (i.e. common-gate) configurations were realized from the same BP transistor. The voltage bias was at a symmetric value of V_{gs}=-1.6V and V_{ds}=-2V, where the intrinsic gain (g_m/g_{ds}) for the device was around its peak value. The output characteristics of the device was shown in Fig. 3.7 (a) with V_g bias increasing from -1.5V to -2.2V from bottom to top at a step size of -0.1V. Strong saturation was observed. The intrinsic gain for this transistor device was extracted as shown in Fig. 3.7 (b). Peak intrinsic gain for V_g=-1.5V to -2.2V are within 25-28. The highest intrinsic gain of 28 was reached at V_g=-1.6V and a drain bias of V_d=-2.1V, which were then chosen as the bias conditions for both inverting and non-

inverting ambipolar amplifiers (Fig. 3.8(b) and (c)). Geometry for this transistor device is W/L=10.6μm/2.7μm, with flake thickness of 15nm. Transconductance ($g_m=dI_d/dV_g$) and output resistance or inverse output conductance $(g_{ds}=dI_d/dV_d)^{-1}$ for the same device were extracted as shown in Fig. 3.7 (c) and (d).

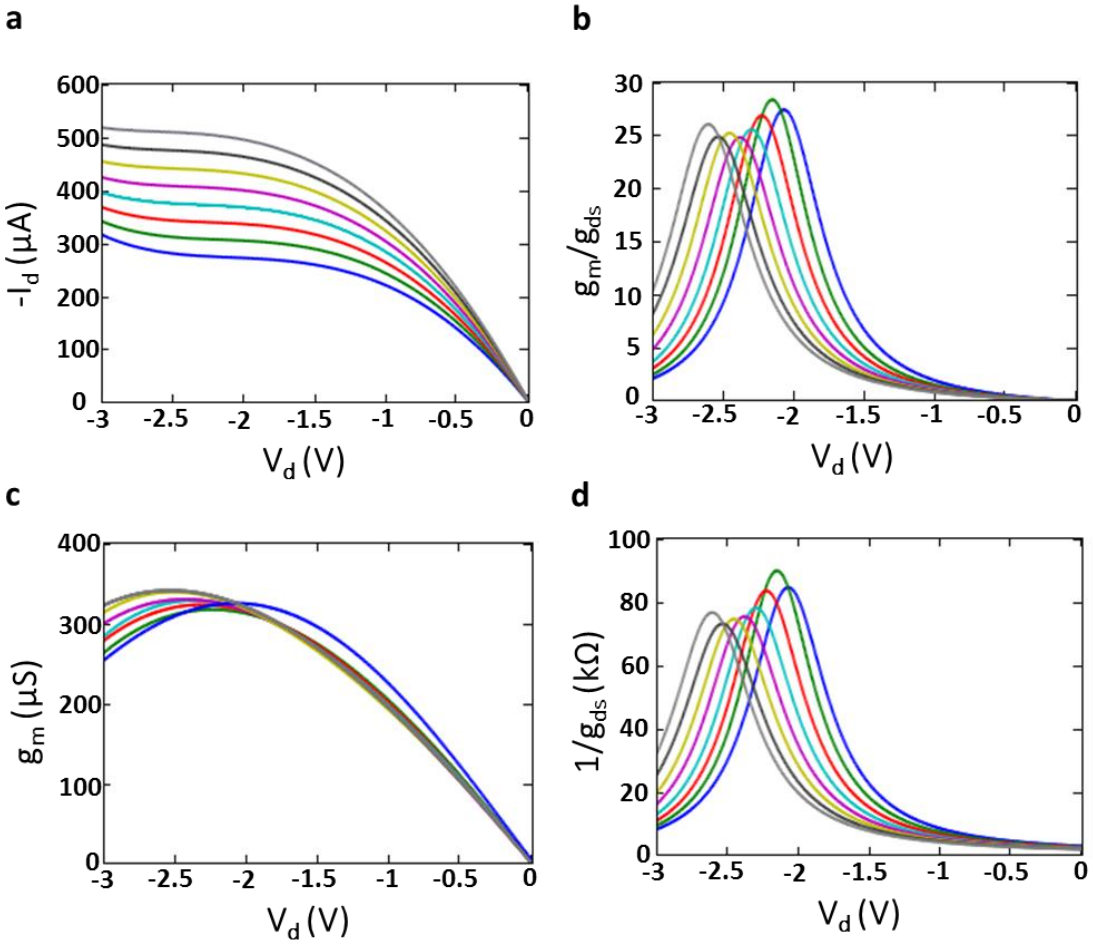

Figure 3.7: Measured intrinsic gain (g_m/g_{ds}) of flexible BP transistor, which provides guidance for selection of the optimum bias conditions for inverting and non-inverting amplifiers.

For the inverting amplifier, the source was grounded and the output collected at the drain terminal, which resulted in a voltage gain ($A_v=V_{out}/V_{in}$) of -8.7 with a small-signal input of V_{pp}=20mV applied at the gate terminal. The amplifier load consisted of a 1MΩ resistor from the oscilloscope, and a shunt inductor - series capacitor bias-tee network for separating DC and AC signals.[68] For the non-inverting amplifier (Fig. 3.8(b)), the bottom gate was grounded and the source and drain served as the input and output terminals respectively, resulting in positive voltage gain of 8.7 for the same small-signal input and load as described for the inverting amplifier. The identical amplifier gains with opposite polarity reflects the symmetry of the gate-source terminal afforded in a 2D semiconductor, in contrast to a bulk semiconductor where the bulk terminal can introduce significant asymmetry between the common-gate and common-source configurations due to the body effect.[69] Previous flexible thin-film transistor based amplifiers achieved voltage gains < 4,[38, 54, 55] hence, the present BP FETs have the highest circuit amplification factor reported so far, which signifies the promising potential of black phosphorus for flexible analog electronics.

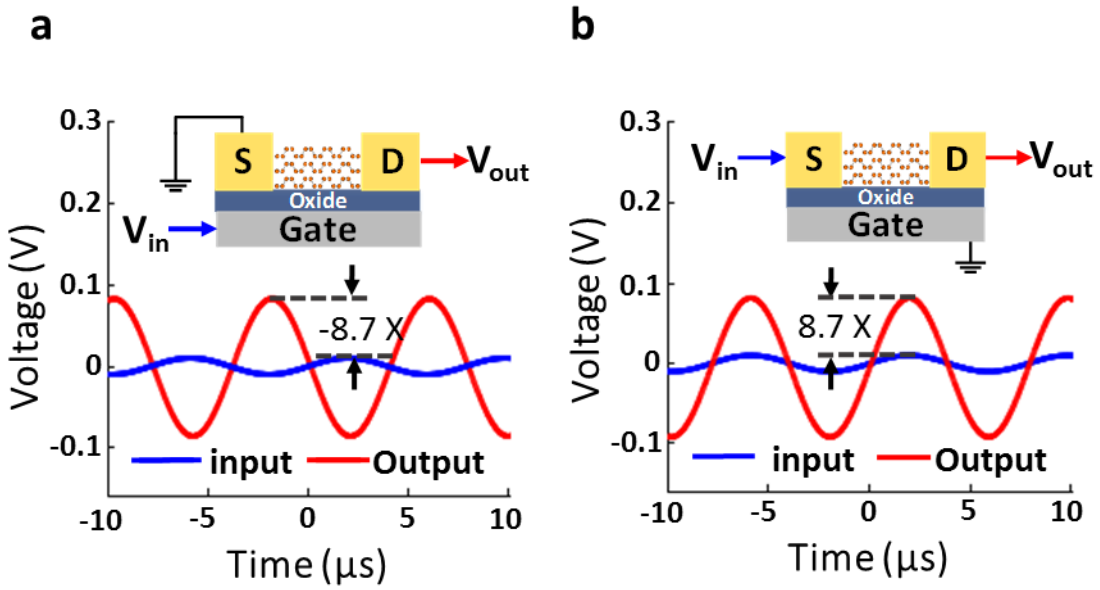

Figure 3.8: (a) Inverting voltage amplifier (i.e., common-source amplifier), and (b) non-inverting voltage amplifier (i.e., common-gate amplifier). At a symmetric DC bias of V_{gs}=-1.6V and V_{ds}=-2.1V for both circuits, the small-signal voltage gain for both amplifiers is ~|8.7|. Simplified AC signal schematics of the device circuit and electrical connections are shown in the inserts.

Flexible BP Frequency Doubler

Single transistor frequency doubler is highly desirable for analog circuits owing to the benefits of low transistor count, reduced power consumption, and the absence of device matching, a stringent requirement for frequency multipliers based on transistor pairs.[70] Previously, graphene frequency doublers based on the square-law ambipolar property of Dirac Fermions have been shown to be suitable for single-transistor frequency doubling with a substantially cleaner output spectrum compared to conventional diode or transistor multipliers that are based on current-voltage non-linearities.[30, 71, 72] Here, we demonstrate for the first time that flexible BP transistors can suitably function as a single-transistor frequency doubler based on the ambipolar charge transport of elementary Fermions (see supplementary information for the analysis of ambipolar BP frequency doubler). The main distinction between ambipolar black phosphorus and ambipolar graphene (under ideal electron-hole symmetry) arises at the ambipolar symmetry point that reflects a diffusive (exponential) transport for black phosphorus, and a drift (linear) transport for graphene. While graphene can afford a higher conversion gain due its more optimum square-law properties,[71] black phosphorus can offer lower power and higher power efficiency owing to its lower off current and DC power dissipation, respectively. Our primary purpose here is to investigate frequency doublers based on black phosphorus and subsequently exploit the ambipolar property for realizing an AM demodulator on a flexible substrate, of great importance for communication and connectivity in future flexible smart systems.[27]

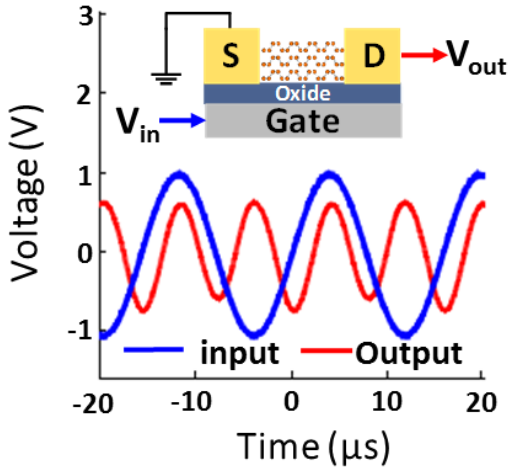

Figure 3.9: Ambipolar single FET frequency doubler. Input signal is 64 kHz sinusoid with V_{pp}=2V. Output signal oscillates at the double frequency (128 kHz) with a voltage gain of ~0.7. V_g=0V and V_d =-1V.

For frequency doubler operation, the BP transistor device shown in Fig. 3.9 was biased at V_d=-1V to realize a more symmetric transfer characteristic near the minimum conduction point, V_{min}=0.54V, which was slightly adjusted to V_g=0V to account for the asymmetry between electron and hole transport, similar to previous report on asymmetric graphene frequency doubler.[73, 74] Sinusoidal frequency doubling was achieved with a conversion gain of 0.72 between output and input voltages with the input frequency at 64kHz and an input V_{pp} of 2V as shown in Fig. 3.9.

Flexible BP AM Demodulator

Based on the ambipolar property of our BP transistors and the above-mentioned realization of frequency doubler, we developed a flexible BP AM demodulator. The BP AM demodulator is a single-transistor circuit that demodulates AM signals, which can be monitored electrically via an oscilloscope or acoustically via a loudspeaker. The measurement system setup is provided Fig. 3.10.

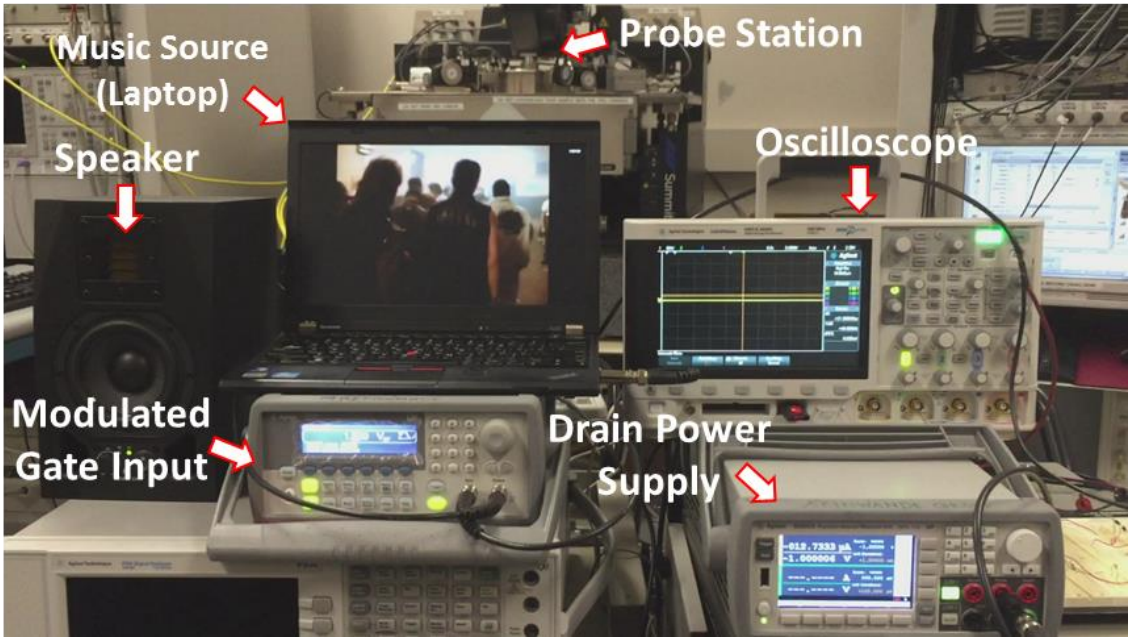

Figure 3.10: Picture of the flexible BP AM demodulator measurement setup.

Future flexible BP AM radio receiver[75] can be realized based on our successful demonstration of an AM demodulator, the schematic of which is shown in Fig. 3.11(a). BP transistor was biased at V_g=0V and V_d=-1V, the same conditions as the frequency doubler. The 2nd-order square law demodulator analysis of ambipolar black phosphorus is detailed in the supporting information. Baseband audio signal was AM modulated onto a carrier frequency (55kHz) as input to the gate terminal, while the output demodulated signal at the drain terminal was sent either to a loudspeaker or an oscilloscope. To elucidate the square law demodulator performance of the flexible BP AM demodulator, a 5kHz sinusoidal baseband signal was applied and its corresponding output spectrum was evaluated using an oscilloscope with high resolution fast Fourier transform (FFT). With the same DC bias as mentioned earlier and with varying carrier signal amplitude from 100mV to 800mV, the output amplitude of the demodulated 5kHz signal increased quadratically in agreement with the expected square law behavior as is shown in Fig. 3.11(b). In addition, the linear

dependence of the baseband output amplitude on the modulation index was observed as expected for a square law device (Fig. 3.11(c)). The FFT output signal spectrum for a 100mV input peak-to-peak carrier amplitude at 100% modulation index is shown in Fig. 3.11(d). The carrier feed-through present in the spectrum is due to the asymmetry of the BP ambipolar transistor, consequently resulting in odd harmonics.[71]

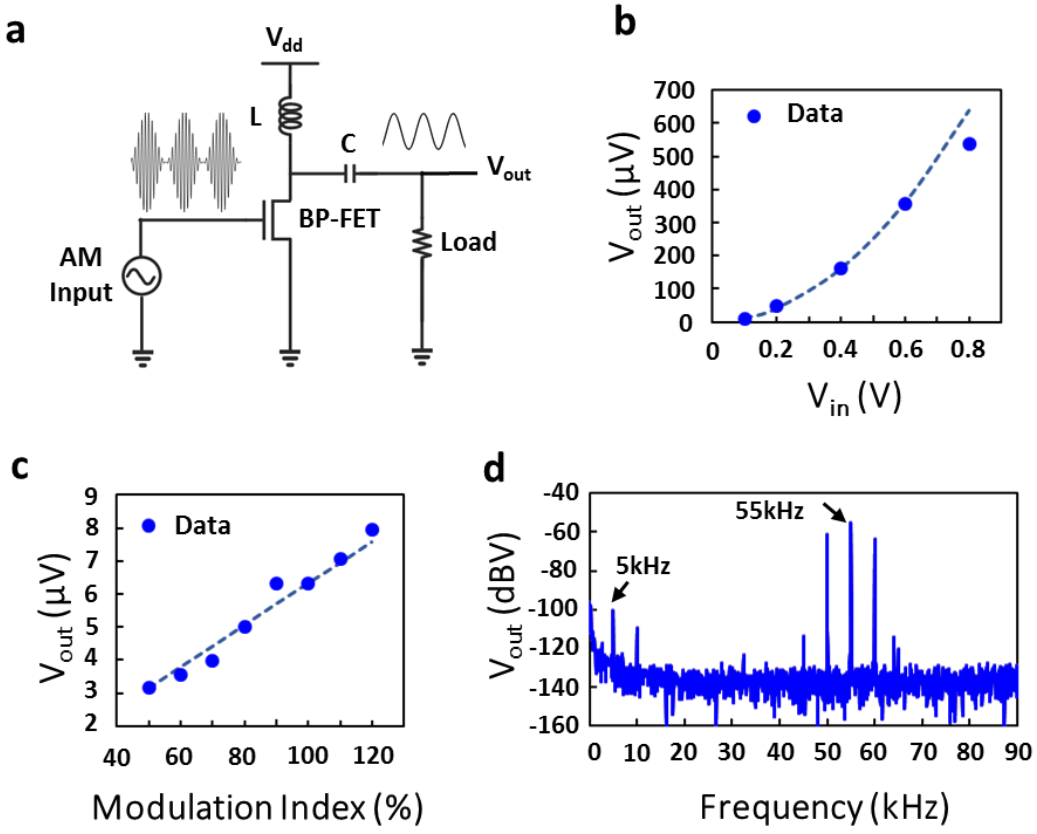

Figure 3.11: Demonstration of an AM demodulator based on flexible BP FET. (a) Schematic representation of an ideal AM demodulator system based on BP FET operating at the ambipolar point. An AM modulated low-frequency signal constituted the input drive to the gate of the ambipolar FET. BP FET at the ambipolar point can be approximated to 2^{nd}-order as a square law device resulting in self-mixing that produces a demodulated output that can be observed in an oscilloscope or heard via a loudspeaker. (b) Dependence of demodulated baseband output (5KHz sinusoid) on V_{pp} of the input carrier signal (55KHz sinusoid). The symbols are the measured demodulated output signal dependence, which is in agreement with the expected square-law quadratic relation indicated by the dashed line. (c) Dependence of the demodulated output baseband signal on the modulation index displays a linear trend (dash line) as expected from square law demodulator theory. (d) Output spectrum of the ambipolar transistor demodulator showing the demodulated baseband signal (5KHz) and the modulated carrier feed-through (55KHz). Input carrier V_{pp}=100mV.

MECHANICAL ROBUSTNESS OF FLEXIBLE BP THIN-FILM TRANSISTORS

In addition to device and circuit performance, transistor robustness under applied strain is another criterion of central importance for flexible electronics. In this work, the robustness of flexible BP transistors and demodulator with respect to both uniaxial tensile strain loading and multi-cycle bending were evaluated for the first time. All the electrical characteristics were measured ex-situ (after the applied strain was released), a straightforward and conventional method for evaluating the mechanical robustness of flexible devices.[29, 32, 76] In this work, crystal orientation dependent transport anisotropy was not considered due to the range of tensile strain applied (≤2%), which is not expected to result in significant crystal orientation dependent device performance. [13, 77, 78]

With uniaxial tensile strain applied, it is necessary to compare the effect of parallel ($\varepsilon_{\parallel}$) and perpendicular ($\varepsilon_{\perp}$) strains on flexible BP transistors. $\varepsilon_{\parallel}$ ($\varepsilon_{\perp}$) is defined as the case when the uniaxial tensile strain is aligned parallel (perpendicular) to the direction of electrical transport in the transistor. The transfer characteristics measured after 1.5% tensile strain for both $\varepsilon_{\perp}$ (Fig. 3.12(a)) and $\varepsilon_{\parallel}$ (Fig. 3.12(b)), reveal stable device properties with $\varepsilon_{\parallel}$

showing a slightly higher effect on device characteristics resulting in a relatively larger shift in both the threshold voltage (V_t) and V_{min}. One plausible reason for this effect is the significant reduction of local longitudinal strain in BP channel induced by $\varepsilon_{\perp}$ compared to $\varepsilon_{\parallel}$ due to the Poisson effect.[79, 80] The Poisson ratio of the polyimide substrate is ~0.34. Moreover, in the transfer characteristics measured after 1.5% parallel tensile strain, no significant change in the basic device parameters such as I_{on}, current on/off ratio and carrier mobility has been observed. The extracted mobility variation from Fig. 3.12(b) is within 3.7% of its initial value.

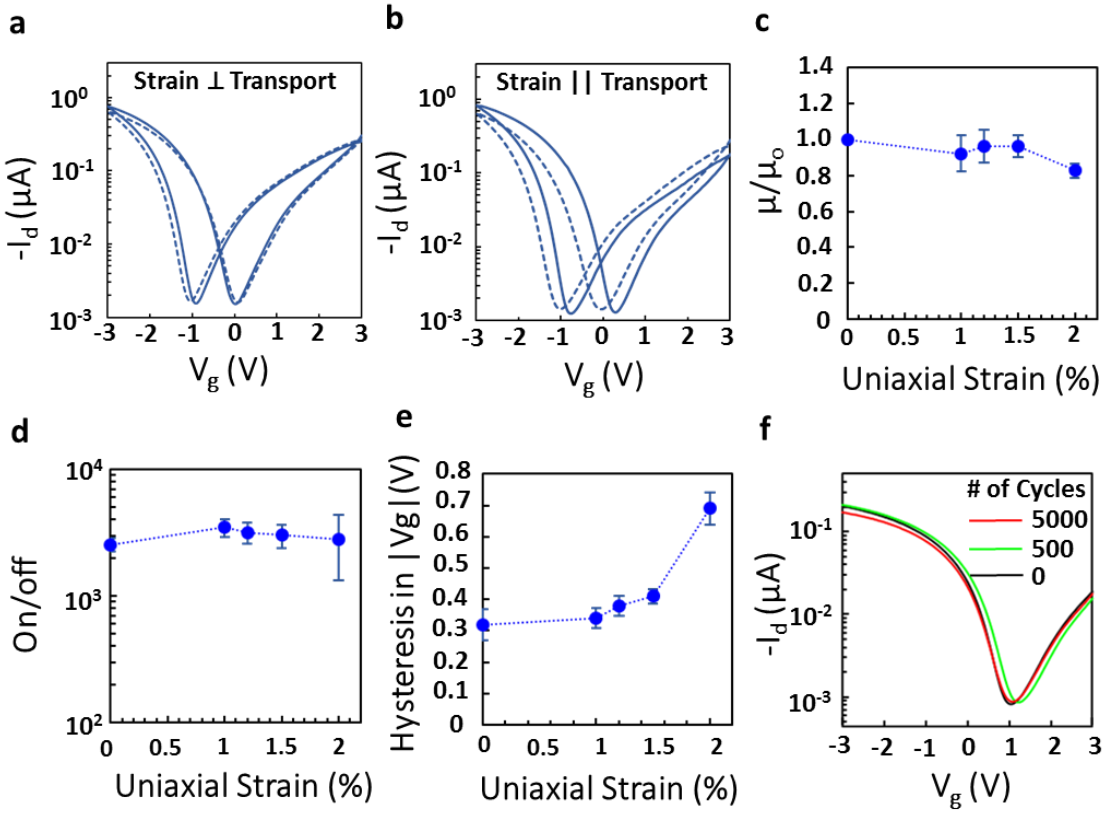

Figure 3.12: Uniaxial tensile evaluation of BP flexible transistors under mechanical bending. (a) and (b) are comparison between transfer curves before (solid line) and after (dash line) applied perpendicular ($\varepsilon_{\perp}$) and parallel ($\varepsilon_{\parallel}$) uniaxial tensile strain of ~1.5%, respectively. Larger hysteresis was observed when the applied strain is parallel to the direction of charge transport. Device statistics including (c) normalized low-field hole mobility μ_h, (d) on/off ratio, and (e) voltage hysteresis under increasing tensile strain in the parallel direction ($\varepsilon_{\parallel}$). Device performance degradation begins at ~2% strain, which is attributed to residual strain in the substrate and the Al_2O_3 gate dielectric and passivation layers. (f) Multi-cycle 3-point bending results, showing the robustness of BP device transfer characteristics before and after 500 and 5,000 bending cycles. The BP devices were at the center of curvature of the substrate for the bending experiments.

To further investigate the performance robustness of flexible BP transistors, transfer and output characteristics were evaluated under increasing tensile strain $\varepsilon_{\parallel}$, which will result in higher effect on device performance as above-mentioned, up to 2% corresponding to 3mm bending radius. Statistics for electrical parameters of interest, including normalized mobility, on/off ratio, and hysteresis in V_g are shown in Fig. 3.12(c), (d) and (e), respectively. Low-field mobility was impacted by less than 5% on average till ~1.5% strain. At about 2% strain, the average normalized mobility reduced by ~18% indicating a more pronounced performance degradation (Fig. 3.12(c)). Similar trends were observed for the on/off ratio and voltage hysteresis. While the average on/off ratio remained relatively stable under bending strain as is shown in Fig. 3.12(d), the standard deviation increased noticeably at the maximum applied strain of 2%. For hysteresis in V_g (Fig. 3.12(e)), the average value increased from ~0.3V to ~0.4V at strains up to 1.5%, and to ~0.7V at 2% strain. We attribute the observed degradation of BP device robustness at ~2% strain to the 25nm Al_2O_3 dielectrics (bottom gate dielectric and top-side encapsulation), which is known to suffer from film degradation at tensile strains ~≥2%.[32] Moreover, 2% applied tensile strain is above the elastic-plastic transition point (i.e., yield strain) of the PI substrate, hence, the substrate cannot fully recover after release of the

strain.[81] Residual strain in the PI substrate can result in increased interface trap charge in the gate dielectric, consequently leading to reduced mobility, on current, drain current modulation, and increased hysteresis.[82-84] We note that the mechanical robustness of BP devices can be further improved by utilizing flexible insulators such as two-dimensional h-BN and organic insulators,[29, 30, 33, 85] as dielectric and passivation layers.

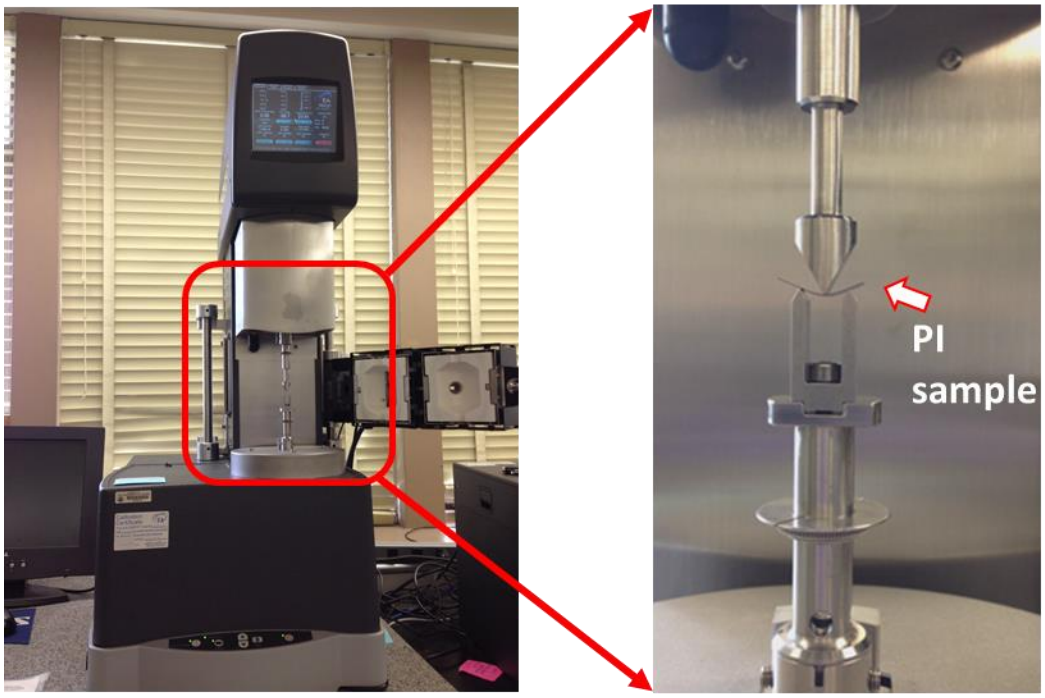

Figure 3.13: RSA-G2 Dynamic Mechanical Analyzer (DMA) with 3-point bending fixture (zoom-in figure) employed for repeated bending up to 5000 cycles at a bending frequency of 1Hz.

For practical flexible and bendable electronics, another important criterion is the device endurance under repeated bending. In this work, an RSA-G2 Dynamic Mechanical Analyzer **(**DMA) was applied for multi-cycle 3-point bending measurements. The DMA system setup is shown in the supporting information Fig. 3.13. and the working scene can be seen in supporting video 2. A tensile strain of 1.5% was applied to the BP transistors.

500 and 5,000 cycles with bending frequency of 1Hz were applied and no mechanical failure was observed. As is shown in Fig. 3.12(f), the transfer characteristics of the flexible BP transistors demonstrated strong stability even after 5,000 cycles of bending. To further verify the robustness of flexible BP electronics, we re-measured the demodulator after 500 cycles of bending, showing that in addition to the current-voltage characteristics, the demodulation functionality was also preserved with similarly high demodulation efficiency.

CONCLUSION

In summary, we have investigated semiconducting BP devices on flexible substrates for the first time and achieved high mobilities, inverting and non-inverting amplifiers, and frequency doubler. The experimental BP transistors showed robust performance under mechanical bending up to ~2% tensile strain and 5000 bending cycles. Larger mechanical strains can be accommodated by replacing commonly used high-k dielectric with flexible organic or polymeric gate dielectric. Furthermore, we demonstrate a flexible AM demodulator, enabled by a single BP ambipolar transistor. Our device results on polyimide represent the state-of-the-art in electronic performance among layered semiconductor flexible transistors.

Chapter 4: Flexible Black Phosphorus GHz Transistors

(Reproduced with permission from W. Zhu, S. Park, Y. Yogeesh, K. M. McNicholas, S. R. Bank, and D. Akinwande, "Black Phosphorus Flexible Thin Film Transistors at GHz", *Nano Lett,* vol. 16, pp. 2301-6, Apr 13 2016)

Weinan Zhu, Saungeun Park, Maruthi N. Yogeesh, Kyle M. McNicholas, Seth R. Bank

*and Deji Akinwande**

†Microelectronics Research Center, Department of Electrical and Computer Engineering, The University of Texas at Austin, Austin, TX, 78758, USA.

ABSTRACT

Black phosphorus (BP) has attracted rapidly growing attention for high speed and low power nanoelectronics owing to its compelling combination of tunable bandgap (0.3 eV to 2 eV) and high carrier mobility (up to ~1000 $cm^2/V{\cdot}s$) at room temperature. In this work, we report the first radio-frequency (RF) flexible top-gated (TG) BP thin-film transistors on highly bendable polyimide substrate for GHz nanoelectronic applications. Enhanced p-type charge transport with low-field mobility ~233 $cm^2/V{\cdot}s$ and current density of ~100 μA/μm at V_{DS}=-2 V were obtained from flexible BP transistor at a channel length L=0.5 μm. Importantly, with optimized dielectric coating for air-stability during microfabrication, flexible BP RF transistors afforded intrinsic maximum oscillation frequency f_{MAX} ~ 14.5 GHz and unity current gain cut-off frequency f_T ~17.5 GHz at a channel length of 0.5 μm. Notably, the experimental f_T achieved here is at least 45% higher than prior results on rigid substrate, which is attributed to the improved air-stability of

fabricated BP devices. In addition, the high frequency performance was investigated through mechanical bending test up to ~1.5% tensile strain, which is ultimately limited by the inorganic dielectric film rather than the 2D material. Comparison of BP RF devices to other 2D semiconductors clearly indicate that BP offers the highest saturation velocity, an important metric for high-speed and RF flexible nanosystems.

INTRODUCTION

Two dimensional (2D) atomic layered semiconductors have been widely studied as promising candidates for flexible nanosystems with functionalities ranging from sensing to wireless communication owing to their compelling electrical, optical and mechanical properties, including ultimate thickness scalability down to one atomic layer, ideal electrostatic control and superior mechanical flexibility with strain limit >20%.[7-9, 27, 29, 35-37, 44, 46] As the most studied 2D layered nanomaterial, graphene with high carrier mobilities (~10,000 cm^2/Vs at room temperature) is most promising for ultra-high frequency analog nanosystems, such as THz detectors.[4, 29] The zero bandgap semimetal nature of graphene, however, results in low field-effect modulation and high OFF state current limiting its applications for logic and low power nanoelectronics. On the other hand, semiconducting transition metal dichalcoginides (TMDs) offer sizeable band gaps with large ON/OFF current ratio (~10^7) that is favorable for low power electronics and digital circuits. However, their relatively low room temperature carrier mobilities (10-100 cm^2/Vs) limit their prospects for high frequency applications.[12, 32, 40, 86] With the emerging needs for both high speed and low energy consumption in flexible nanosystems, few-layer black phosphorus (BP), phosphorene as its monolayer counterpart, has been rediscovered as a promising candidate to combine the fast transport of graphene and the high band gap of TMDs such as high room temperature carrier mobility ~1000 cm^2/Vs [15] and highly

sensitive thickness-dependent direct bandgap from 0.3 eV (bulk) to 2 eV (monolayer).[16, 19, 53, 87]

In this work, we present the first realization of flexible top-gated (TG) BP transistors with intrinsic current gain frequency, f_T~17.5 GHz and power gain frequency, f_{MAX}=14.5 GHz achieved at a channel length L= 0.5 μm. Another device with the same channel length that afforded intrinsic f_T~20 GHz provides an indication of the reproducibility of our flexible BP transistors. Despite the many challenges experienced, such as lack of precise control of size, thickness and orientation of BP films, and the difficulties of device integration on non-atomically smooth low-thermal budget soft substrates, the compelling performance obtained from the first investigation of BP based flexible RF transistors demonstrates the potential for this emerging 2D layered semiconductor for flexible smart nano systems. Bending test was conducted to investigate the high frequency performance of the flexible TG BP transistors with extrinsic f_T measured under tensile strain up to 1.5%, invariably limited by the relatively stiff high-κ atomic layer deposited (ALD) dielectrics.[32]

RESULTS AND ANALYSIS

Fabrication and Characterization of Flexible Top-gated BP Transistor

In this work, mechanically exfoliated black phosphorus flakes with typical thickness of 10 to 25 nm were selected as the semiconducting channels.

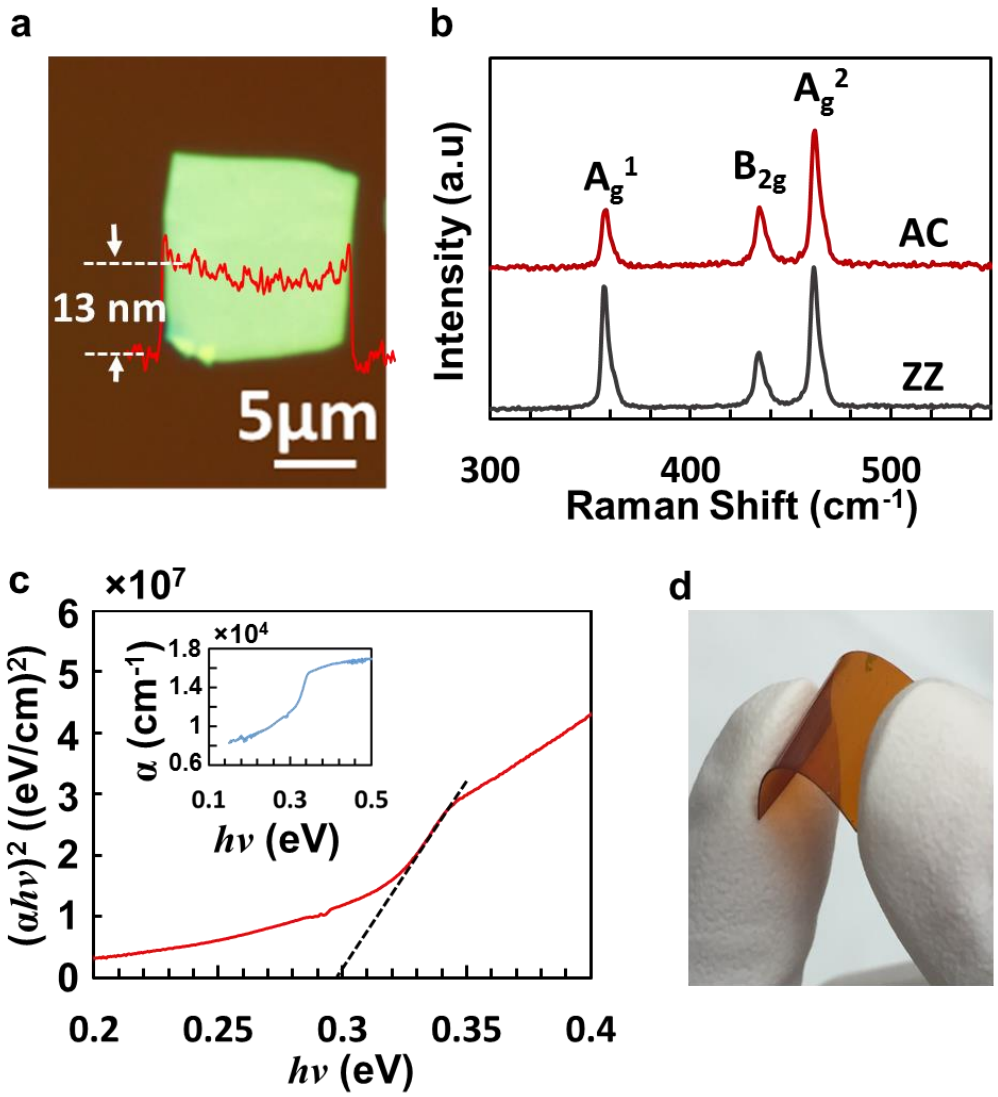

Figure 4.1: (a) Optical image of multi-layer BP flake with uniform thickness of 13 nm as determined by atomic force microscopy (AFM) shown as the red line. (b) Raman spectrum of a typical BP flake with incident laser polarization within a close affinity to arm-chair (AC) and zig-zag (ZZ) directions, respectively. 532 nm green laser was used to obtain the Raman spectrum. (c) A representative Tauc plot for estimating the optical bandgap, which confirms a gap of ~0.3 eV in the bulk limit. Insert is the absorption coefficient of BP derived from Fourier transform infra-red (FTIR) spectrum. (d) Picture of fabricated flexible TG BP devices on highly bendable PI substrate.

Optical microscopy image of a typical BP sample is shown in Figure 4.1(a), with uniform thickness ~13 nm verified by atomic force microscopy (AFM). The crystalline nature of BP was verified by Raman spectroscopy with incident laser (λ=532 nm) polarized along both armchair (AC) and zigzag (ZZ) directions, as shown in Figure 4.1(b), where ratio among characteristic peaks of A_g^1, B_{2g}, and A_g^2 clearly inidcate the in-plane orientations.[14, 16] For exfoliated BP flakes with thickness more than 10 nm, the theoretical bandgap is ~0.3 eV,[53] which is confirmed in Figure 4.1(c) by Fourier transform infrared (FTIR) spectroscopy that is represented as a Tauc plot ($(\alpha h\nu)^2 = h\nu - E_g$),[21, 88] an established method for determining the optical band gap. $h\nu$ is the photon energy, E_g is the optical bandgap, and α is the absorption coefficient. As shown in Figure 4.1(d), highly bendable Kapton polyimide (PI) sheets ~125 μm thick were adopted as the substrate for the flexible BP transistors with double sided solution-based PI thin film coating and curing process applied to smoothen the substrate to about 1 nm surface roughness.[29, 32, 58] A 25 nm Al_2O_3 dielectric thin film was then deposited using atomic layer deposition (ALD) at 250 °C on top of the PI substrate to provide: i) a high-k environment for enhancing carrier mobility by suppressing charge impurity scattering,[32, 89] and ii) better adhesion between the BP channel material and the substrate.

To fabricate the flexible TG BP transistors as illustrated in Figure 2(a), the source and drain metal contacts were defined by electron beam lithography (EBL) followed by electron beam evaporation of Ti/Au=1.5 nm/50 nm with Au selected to enhance the p-type transport due to its relatively large work function.[90] Subsequently, 25 nm of Al_2O_3 was deposited again at 250 °C to serve as the high-κ top-gate dielectric. TG electrodes were formed by EBL followed by e-beam evaporation of Ti/Au=1.5 nm/50 nm. Here, a dual-finger TG structure with an underlap configuration was adopted to enhance the current transport as well as to reduce parasitic capacitance between TG and S/D electrodes.[29, 32, 91]

In order to preserve the pristine electrical properties of the flexible TG BP transistors, ambient exposure time of hygroscopic BP channel[22, 23] was minimized during the aforementioned nanofabrication process by: i) immediate polymethyl methacrylate (PMMA) coating after the exfoliation of the BP flakes onto the flexible PI substrate, where PMMA layer functions as both an effective encapsulation layer for BP characterization and the e-beam resist for subsequent device fabrication; and ii) immediate ALD deposition of 25 nm Al_2O_3 after S/D metal liftoff process, where the Al_2O_3 layer functions as both TG dielectric and the encapsulation layer.[22, 23, 90]

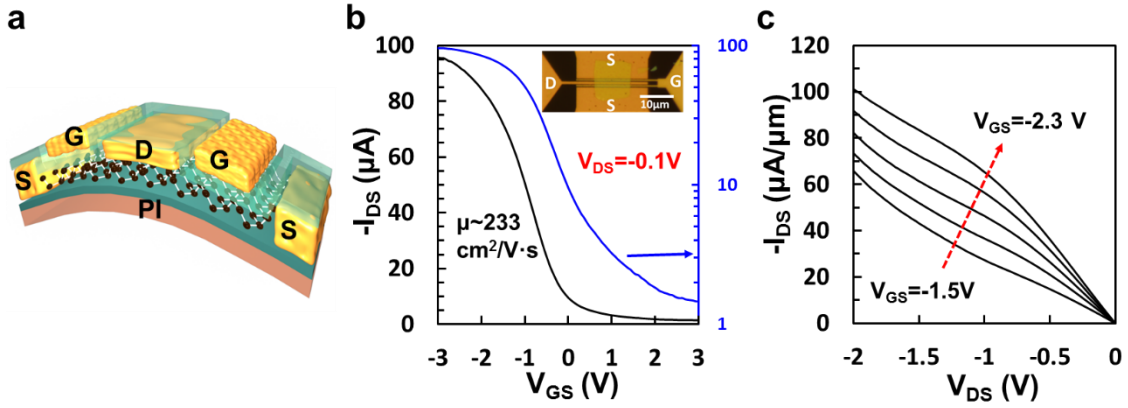

Figure 4.2: Flexible top-gate BP transistor structure and DC performance at 300 K. (a) Illustration of flexible TG BP transistor. Dual-finger TG structure was adopted with Ti/Au=1.5 nm/50 nm as both the source/drain and gate electrode stack. 25 nm Al_2O_3 was employed as the TG dielectric as well as the protection layer for air stability. (b) Transfer characteristics of fabricated device featuring high-mobility p-type charge transport. V_{DS}=-0.1V. The extracted low-field hole mobility ~233 $cm^2/V{\cdot}s$. (c) Output characteristics of the same device showing soft current saturation. The W/L=10.8 μm/0.5 μm, and flake thickness is 13 nm.

Enhanced p-type current transport was obtained from the DC characteristics of the flexible TG BP transistors as shown in Figure 4.2(b) and (c). The transport measurements were conducted using a Cascade probe station and an Agilent 4156 semiconductor parameter analyzer. Low-field hole mobility μ_p~233 $cm^2/V \cdot s$ was extracted using the Y-function method[62] from the transfer characteristics, as shown in Figure 4.2(b), which is comparable with prior works of bottom-gated (BG) flexible BP transistors[90] and TG BP transistors on rigid Si substrates.[91] The contact resistance, R_c~4.5-6.7 $k\Omega \cdot \mu m$ was also extracted simultaneously via Y-function method, which is ~1/3 of the total channel resistance R_{total}~16-17 $k\Omega \cdot \mu m$ and as such, it is not the dominant factor in charge transport. The current modulation is within 10^2 and agrees well with our prior studies of BP transistors fabricated from flakes with thickness around 13 nm to 15 nm.[26, 28] The relatively low current modulation is attributed to fixed surface charge induced by the ALD top gate dielectric deposition process[92] and the small band gap (~0.3 eV) of the relatively thick 13 nm BP flake.[34] The transconductance (g_m) of the same device under drain bias of V_{DS}=-0.1 V is shown in Fig. 4.3, with peak value g_m~56.7 µS obtained at V_{GS}=-0.72 V. The high mobility value and transconductance obtained from this first realization of flexible top-gate BP transistors indicate strong potential for higher frequency applications beyond TMDs.

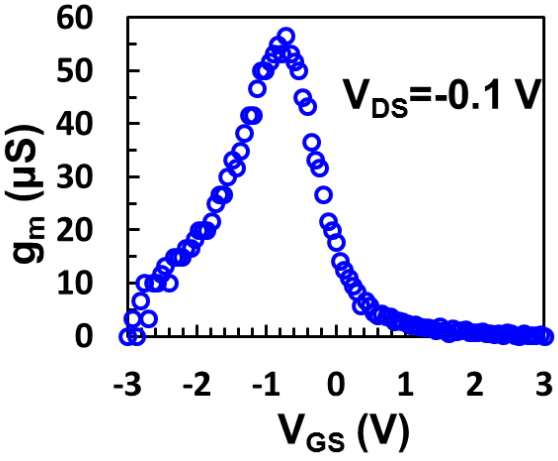

Figure 4.3: Low-field transconductance (g_m) of flexible TG BP transistor with V_{DS}=-0.1 V. Peak g_m~56.7 μS was obtained at V_{GS}=-0.72 V. W/L=10.3 μm/0.5 μm.

The output characteristics of the same flexible TG BP transistor are shown in Figure 4.2(c). The highest current density obtained from the output characteristics is ~100 μA/μm under bias conditions of V_{DS} =-2 V and V_{GS}=-2.3 V. The output current saturation, however, was not as strong as our prior study of flexible BG BP transistors,[90] which we attribute primarily to contact resistance R_c resulting from the ungated access region in this underlap TG configuration.[6, 29, 91] This has been previously shown to have the effect of obscuring current saturation in 2D devices.[93, 94] Therefore, with optimized self-aligned TG structure, the access region will be reduced and enhanced current saturation can be expected.

Radio Frequency Performance

The high frequency performance of flexible TG BP transistors was characterized using standard S-parameter technique with Cascade electrical probe station and an Agilent Vector Network Analyzer (VNA-E8361C) up to 30 GHz. GSG probing pads were adopted in the design of flexible TG BP transistors to ensure high frequency signal fidelity. Gate and drain were selected as the pair of transmission electrodes, whereas the source functioned as the ground electrode. To calibrate-out the response of the GSG radio frequency probes and cables, the standard processes of short, open, load and through were followed strictly before moving to the flexible BP transistors.

Unity current gain ($|h_{21}|$) cut-off frequency, f_T, is one of the most important figure-of-merit to evaluate the high frequency prospects of transistor devices.[28, 29, 91] In this work, flexible TG BP transistors with channel length of L=1, 0.5, 0.25 μm were investigated, with the DC characteristics for typical devices of L=1 μm and L=0.25 μm shown in Fig. 4.4 and 4.5, respectively.

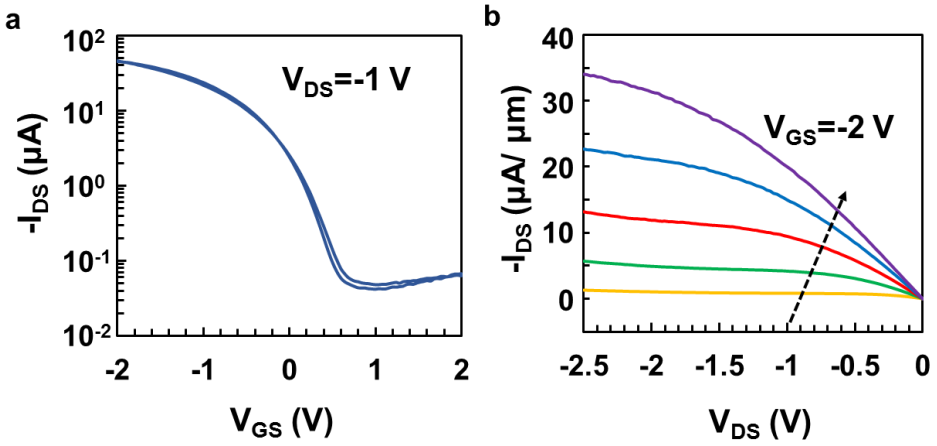

Figure 4.4: DC characteristics of flexible BP FET with channel length of 1 μm in ambient environment at 300 K. (a) Transfer characteristics in log scale at V_{DS}=-1 V. Forward and backward sweep showing negligible hysteresis with On/Off ratio ~ 10^3 was obtained. (b) Output characteristics of the same device showing current saturation. V_{GS}=0 V to -2 V with a step of -0.5 V. W/L=2.6 μm/1 μm.

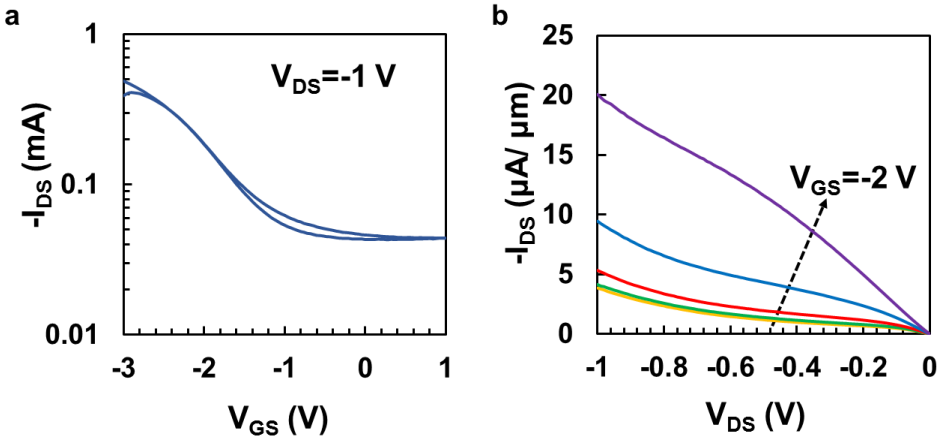

Figure 4.5: DC characteristics of flexible BP FET with channel length of 0.25 μm in ambient environment at 300 K. (a) Transfer characteristics in log scale at V_{DS}=-1 V. Forward and backward sweep showing negligible hysteresis. (b) Output characteristics of the same device. V_{GS}=0 V to -2 V with a step of -0.5 V. BP flake thickness is ~23 nm. W/L=11 μm/0.25 μm.

Here in this work, the physical gated length was taken to be the electrical channel length, which is reasonable justified since Schottky barrier widths at the contacts, typically on the order of nanometers, are much smaller than our fabricated device dimensions.[95] With much shorter Schottky barrier width than the physical (gated) channel length expected in our underlap flexible BP RF device structure, the transistor performance is governed by classical drift-diffusive transport and is not a Schottky-barrier FET.[96] Analysis of the Schottky barrier width of the flexible BP transistor is presented in the Appendix. Strong current saturation is observed in the output characteristics of the device with L=1 μm. The statistics of extrinsic f_T measured for the flexible TG BP transistors with all three channel lengths are shown in Figure 4.6. Here, we attribute the observed extrinsic f_T variations within devices of the same channel length to be due to both extrinsic factors, such as contact resistance and parasitic capacitances, and intrinsic factors such as thickness variations[16, 19, 87] and the strong in-plane anisotropic electrical transport of BP, where the saturation velocity v_{sat} is theoretically projected to vary by a factor of two between the ZZ and AC crystallographic orientations.[97] The latter is a unique property of BP and hence, it is worthwhile to further elaborate on its impact on f_T. Since $f_T \propto v_{sat}$ for RF devices biased under high lateral electrical field condition, the orientation dependent intrinsic f_T can be expressed as $f_T=v_{sat,AC}(1+\cos^2\theta)/4\pi L$, where $v_{sat,AC}$ is the effective saturation velocity along the AC direction, and θ is the in-plane angle between the transport direction and the AC direction. As such, the orientation dependence is expected to result in a two-fold intrinsic f_T device to device variation in randomly oriented BP RF devices.

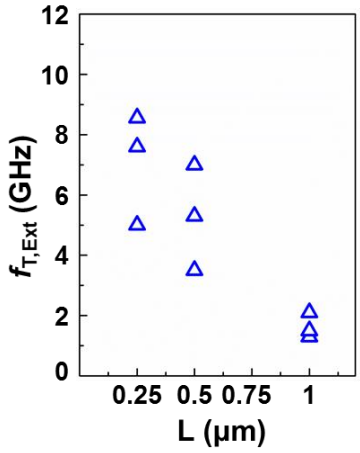

Figure 4.6: High frequency performance of flexible top-gate BP RF transistors. (a) Statistics of extrinsic cutoff frequency of flexible BP RF transistors with channel lengths of 0.25, 0.5 and 1 μm. The sources of device to device variation include extrinsic contributions (e.g. contact resistances and parasitic capacitances) and intrinsic contributions such as the anisotropic orientation dependence that is unique to BP. Further research is warranted to minimize device to device variations in emerging 2D materials.

Further research on device statistics will be most beneficial in elucidating the variation imposed by this unique in-plane anisotropy present in BP and minimizing both the extrinsic and intrinsic sources of device variability. Additional high frequency results of device with channel length of L=0.25 μm are available in Fig. 4.7.

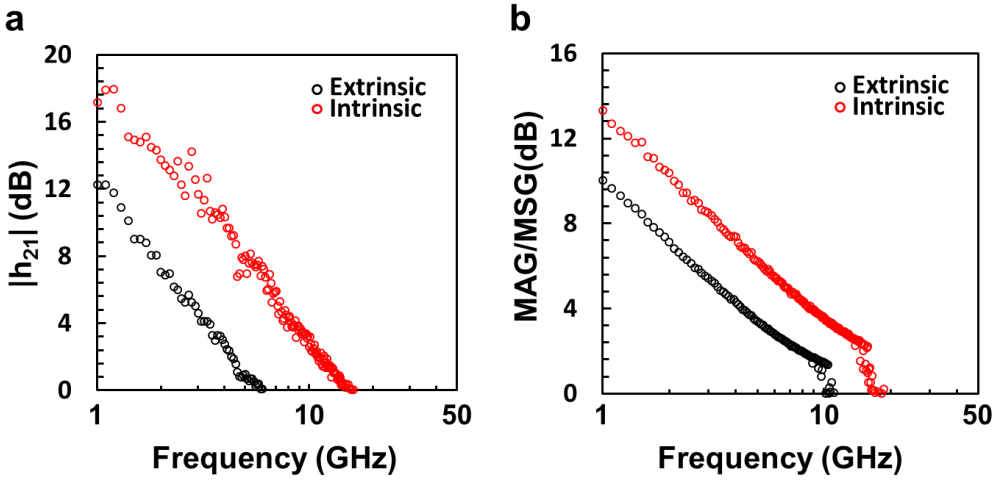

Figure 4.7: High frequency performances of flexible BP transistor with channel length of 0.25 μm. (a) The extrinsic and intrinsic current gain $|h_{21}|$ spectrum of a device with channel length L=0.25 μm. (b) The extrinsic and intrinsic power gain spectrum of the same device.

To further evaluate the potential of high frequency flexible TG BP transistors, the intrinsic high frequency performances of the BP active region were determined through standard open and short de-embedding process.[29, 91] It is worth noting that the channel semiconductor was absent in the open and short structure. As a result, the metal-BP interface and ungated access regions that comprise the contact resistance are not de-embedded, hence, the extracted intrinsic high frequency metrics are a conservative or lower estimate of the BP semiconductor performance on flexible substrate.[28] We present the high frequency performance obtained from a typical flexible TG BP transistor with channel length of L=0.5 μm, the DC performance of which were shown in Figure 2(b) and (c). To achieve maximum carrier transport, V_{DS}=-1.8 V was applied to induce high lateral electrical field. The flexible TG BP transistor was biased near its peak transconductance ($g_{m,max}$) point where V_{GS}=-3.7 V. As presented in Figure 4.8(a), the extrinsic f_T value was ~7 GHz. After de-embedding the effect of parasitic capacitances and resistances from the device structure, the intrinsic f_T value was extracted ~17.5 GHz. As shown in Table 1, this intrinsic f_T obtained from the flexible TG BP transistors is 45% higher than the prior works by Wang *et al.*,[91] despite the fact that the prior work was on rigid substrate. To exclude channel length dependence for comparison and circuit design purposes, a channel length normalized metric $f_T \cdot L$ was selected to evaluate the high frequency prospects as listed in Table 4.1. For RF devices operating in high lateral field region, f_T is limited by saturation velocity, which is directly proportional to $f_T \cdot L$, $f_T \cdot L = v_{sat}/2\pi$. In this work, v_{sat} is defined as the effective saturation velocity due to the non-uniform lateral field distributed along the channel.[98, 99] We consider the channel length as the physical gated length for the estimation

of the effective saturation velocity. For the best flexible TG BP device reported in this work, an intrinsic $f_T \cdot L = 8.75$ GHz·μm was obtained, which is more than two times higher than that reported for BP RF transistor on a Si substrate.[91] A similar improvement was obtained for the $v_{sat} \sim 6 \times 10^6$ cm/s. We attribute this improvement to the optimized fabrication process including minimized ambient exposure time as well as hydrophobic encapsulation, which effectively preserves the electrical performance of flexible BP thin film transistors.

Another key metric for evaluating the high frequency performance of transistors is the maximum oscillation frequency, f_{MAX}, which is defined as the frequency of unity power gain. While f_T is closely related to the intrinsic speed performance of mixed-signal and analog transistor circuits, f_{MAX} is regarded as an upper limit for RF circuits where input and output are often investigated in terms of signal power.[28] For this purpose, we investigated both the extrinsic and intrinsic f_{MAX} extracted from the unilateral power gain, U, as shown in Figure 4.8(b). From Figure 4.8(b), the extrinsic and intrinsic f_{MAX} were extracted to be 10.3 GHz and 14.5 GHz, respectively, which validate the potential for BP based flexible RF nano systems.

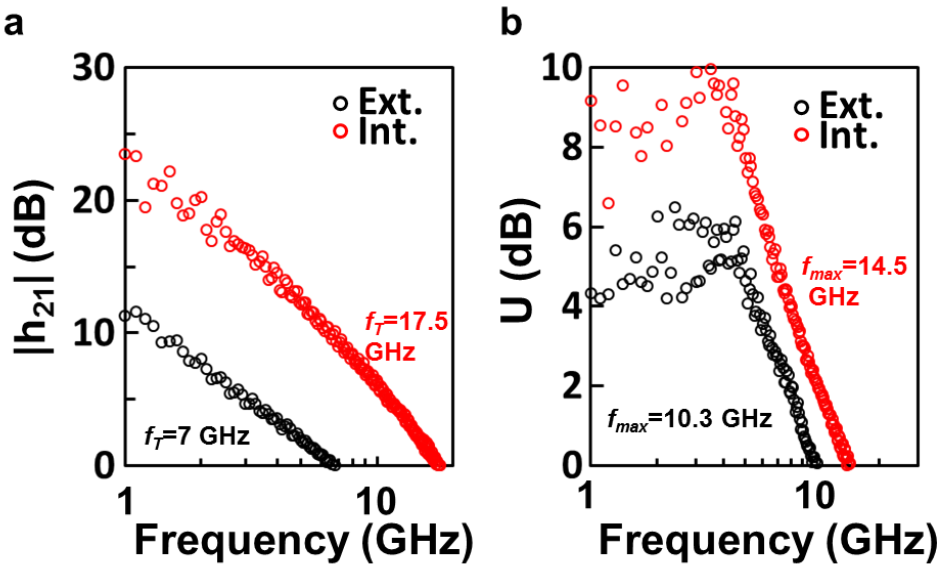

Figure 4.8: Radio-frequency performance of the same flexible BP RF transistor shown in Figure 2 with GHz $f_{T.}$ (a) Short-circuit current gain $|h_{21}|$ before (extrinsic) and after (intrinsic) standard de-embedding. Extrinsic and intrinsic cut-off frequency f_T were extracted as 7 GHz and 17.5 GHz, respectively. (b) Unilateral power gain, U, featuring extrinsic and intrinsic f_{MAX} ~10.3 GHz and 14.5 GHz, respectively. Channel length is 0.5 μm.

The reproducibility of our flexible TG BP transistors is discussed in the Fig. 4.9 and 4.10, where another device with channel length of L=0.5 μm affords intrinsic f_T~20 GHz and f_{MAX}~11 GHz. The AFM images for both devices were shown as the inserts with S, D and G electrodes labeled. Thickness profile was taken along the white dash line. The less symmetric access region observed in Fig. 4.10(b) leads to higher total parasitic capacitance between TG and S/D electrodes, therefore yields a relatively higher intrinsic cutoff frequency f_T after de-embedding.

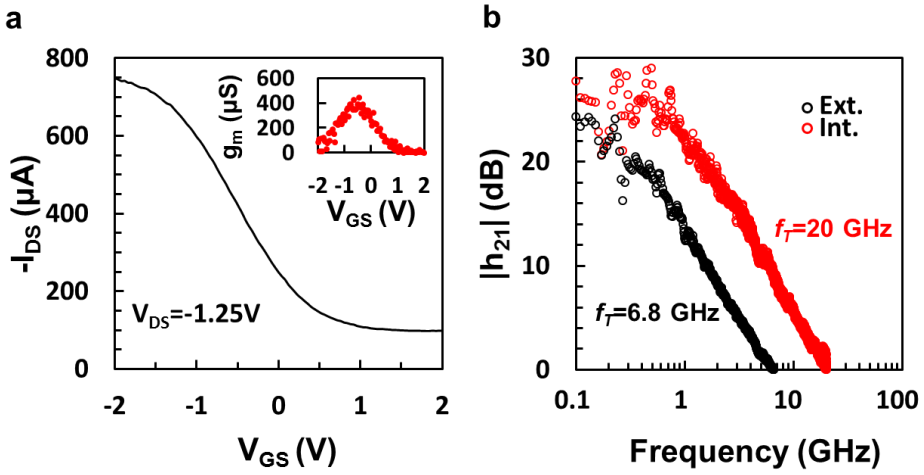

Figure 4.9: DC and high frequency performance obtained from another flexible BP RF device with L=0.5 μm with intrinsic f_T~20 GHz. (a) Transfer characteristics of the device at V_{DS}=-1.25 V. Transconductance is shown as the insert with peak g_m ~400 μS. (b) Short-circuit current gain $|h_{21}|$ before (extrinsic) and after (intrinsic) de-embedding. Extrinsic and intrinsic cut-off frequency f_T were extracted as 6.8 GHz and 20 GHz, respectively. f_{MAX} of the same device before (extrinsic) and after (intrinsic) de-embedding are ~5.8 GHz and 11 GHz, respectively. BP thickness is ~20 nm. W/L=9.7 μm/0.5 μm.

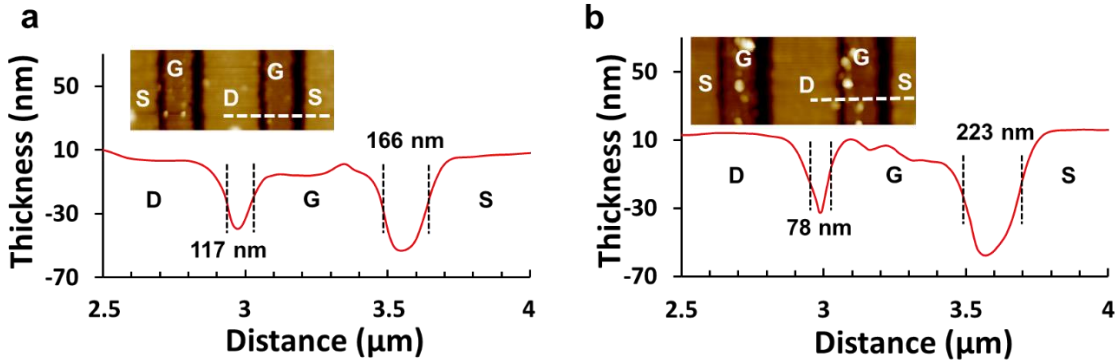

Figure 4.10: AFM analysis of device dimensions of the two flexible TG BP transistors with channel length of 0.5 μm. (a) Access regions between TG and S/D pads were measured to be 166 nm and 117 nm respectively for the device that affords intrinsic f_T~17.5 GHz. (b) Access region between TG and S/D pads was measured to be 233 nm and 78 nm respectively for the device that affords intrinsic f_T~20 GHz.

An insightful comparison of the high frequency performance metrics of f_T, f_{MAX}, $f_T \cdot L$ and v_{sat} among widely studied thin film nanomaterials including BP, few-layer MoS_2, indium gallium zinc oxide (IGZO) and poly-Si are listed in Table 4.1. Flexible top-gate BP transistor demonstrated the highest intrinsic f_T value of ~17.5 GHz with channel length of L=0.5 μm. The extracted saturation velocity is ~6×10^6 cm/s, which is more than one order of magnitude higher than the effective velocities achieved for MoS_2, IGZO and poly-Si.[38, 100-102] As for the maximum oscillation frequency, the flexible TG BP transistor demonstrated f_{MAX}~14.5 GHz which is much higher than those reported for TMDs (e.g. MoS_2), IGZO and poly-Si, which are among the most studied thin film materials for flexible electronics. In addition, graphene and InAs based flexible transistors are also included in Table 1 for comprehensive benchmarking of the state-of-the-art flexible high frequency transistors. However, graphene is rather limited in terms of low power electronic applications due to its lack of a bandgap, and InAs III-V thin-film is intrinsically of limited mechanical flexibility owing to its low strain limit.[5, 10, 27] From this comparison, BP is an outstanding nanomaterial for flexible RF nanosystems and applications.

	Material	**Sub.**	**L (μm)**	**f_T (GHz)**		**f_{MAX} (GHz)**		**v_{sat}* (10^6 cm/s)**	**$f_{T,\,Int}\cdot L$ (GHz·μm)**
				Ext.	**Int.**	**Ext.**	**Int.**		
This work	BP	PI	0.5	7	17.5	10.3	14.5	5.5	8.75
Ref. [91]	BP	Si	0.3	8	12	12	20	2.3	3.6
Ref. [38]	MoS_2	PI	0.068	4.7	13.5	5.4	10.5	0.58	0.92
Ref. [100]	MoS_2	PI	0.5	2.7	5.6	2.1	3.3	0.85	1.35
Ref. [101]	IGZO	Glass	1.5	0.384	-	1.06	-	0.38	0.58
Ref. [102]	Poly-Si	Si	0.2	-	1.1	-	1.6	0.2	0.32
Ref. [5]	Graphene	PET	0.2	32	64	20	34	8.05	12.8
Ref. [10]	InAs	PI	0.075	9.38	105	10.5	22.9	4.95	7.87

*Experimental v_{sat} in this Table is the effective saturation velocity or highest achieved velocity.

Table 4.1: High frequency performance comparison of widely studied 2D and thin film transistors in ambient condition at 300 K.

Mechanical Robustness

In addition to the high frequency performance, the mechanically robustness of the flexible BP transistors was investigated by ex-situ f_T measurements under tensile strain (ε) up to 1.5%. The tensile strain is computed by ε=t/(2r), where t is the overall thickness of PI substrate, and r is the bending radius.[29, 90] For our flexible BP devices, t=150 μm and the bending radius was reduced from 9 mm down to 5 mm, which corresponds to tensile strain up to 1.5%. A typical flexible BP transistor with channel length L=0.5 μm was chosen for this study. As is demonstrated in Fig. 3(b), the extrinsic f_T normalized to the non-strained value was investigated as tensile strain increased up to 1.5%. Strong mechanical robustness was verified with slight performance degradation less than 7% with ε applied up to 1.2%, and the trend is consistent with our previous study on the strain effect on carrier mobility and ON state current of flexible bottom gated BP transistors.[90] With strain increased to 1.5%, much severe performance degradation was observed mainly due to the fracture toughness limitation of high-κ dielectric.[32] This result agrees well with our recent study on BG flexible BP transistors, where 25 nm Al_2O_3 was adopted for both bottom gate dielectric and BP channel encapsulation layer.[90] Similarly in this work, ALD Al_2O_3 was adopted for TG dielectric, the critical strain for which is ~2%.[29, 32, 90] In order to further enhance the mechanical robustness of our flexible BP transistors, optimization of device structure by substituting high-κ dielectric with h-BN[27] or nano scale polymer dielectric[103] are potential solutions.

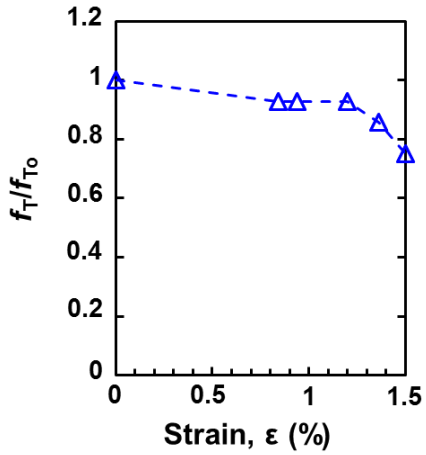

Figure 4.11: Mechanical robustness analysis of flexible TG BP transistor with normalized extrinsic f_T measured under uniaxial tensile strain up to 1.5%. All RF measurement was done ex-situ at 300 K. Blue dash line is a visual guide.

CONCLUSIONS

In this work, we present flexible top-gated BP transistors with high frequency performance including record intrinsic f_T~17.5-20 GHz, intrinsic f_{MAX}~14.5 GHz and high experimental saturation velocity ~6×10^6 cm/s. The effects of the native in-plane anisotropy in BP was considered in the understanding of the channel length dependence suggesting an intrinsic two-fold device to device variation in the effective saturation velocity and the intrinsic f_T. The mechanical robustness of our flexible BP RF transistors was investigated through ex-situ f_T measurements under tensile strain up to 1.5%. Our results indicate that BP offers the highest charge velocities and higher frequency performance compared to other 2D layered semiconductors with a natural band gap making it arguably the most promising layered material for flexible RF nano systems.

Chapter 5: Strain Tunability of 2D Semiconductors

INTRODUCTION

Strain has been long utilized as an effective methodology for tuning the electronic, transport and optical properties of semiconductors for decades.[82, 84, 104-107] As for two dimensional crystals, strain tunabilities are particularly useful due to the fact that 2D layered crystals are able to sustain much higher strains than the bulk crystals due to their intrinsic mechanical flexibility.[77, 108, 109] Graphene and monolayer MoS_2 high purity samples have been reported to have intrinsic strain limit over 15% and 11% without substantially damage to crystal structures.[27] Theoretical studies of few layer BP also indicate a high strain limit of 27% (30%) of uniaxial tensile strain along the ZZ (AC) directions.[17] The large intrinsic strain limit allows for wide range for tuning the electrical properties, such as phonon modes shift, band gap engineering, and even semiconducting-metallic phase change can be observed under sufficient strain loading.[13, 17, 110, 111] Despite the promising predictions by theoretical studies, the practical realization of large strain loading on to 2D crystals so far remains as a big challenge. For highly stretchable systems such as PDMS as the carrier, large Young's modules mismatch between the soft substrate and the stiff 2D semiconductors results in inefficient strain transfer.[112] Also, for flexible devices using high-k dielectric in the structure, such as previously discussed flexible BP transistors, will be strictly limited by the low critical strain dielectric matertials, such as HfO_2 and Al_2O_3.[32, 113]

POLYMERIC LOW-K DIELECTRIC FOR FLEXIBLE SUBSTRATE

To overcome the strain limit of normal high-k dielectric as well as to enhance the strain transfer efficiency, a polyimide based platform for applying uniaxial tensile strain of more than 5% were successfully developed. Here, we adopted thin polyimide sheet with

initial thickness of ~27.5 μm as the flexible substrate. Double sided curing was carried out to smoothen the surface. The mechanical robustness of polyimide substrate was demonstrated in Fig. 5.1, where no slippage occurred until the end-to-end tensile strain reached 20%.

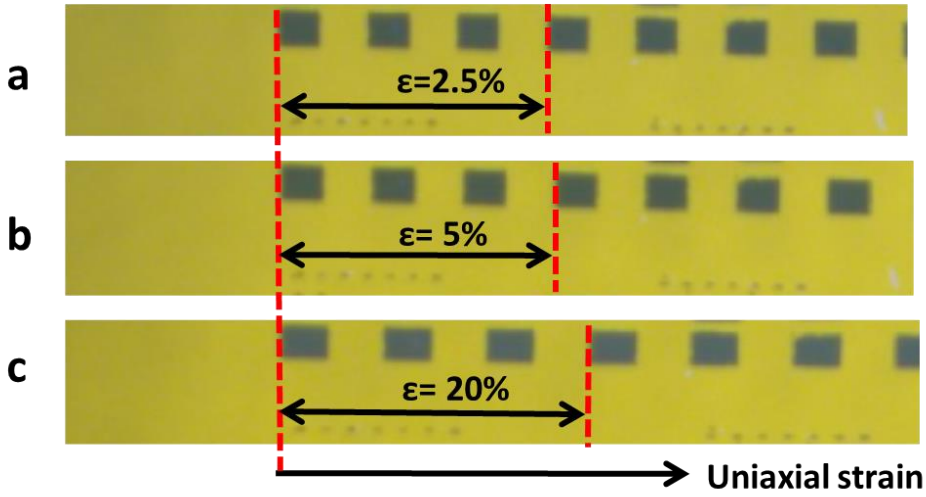

Figure 5.1: Mechanical robustness of polyimide substrate under uniaxial tensile strain.

Ti/Pd metal stack was then e-beam evaporated onto the polyimide substrate to function as the bottom gate as well as Raman signal enhancing layer. Finally, diluted liquid polyimide was spin coated at 6000 ramp/s and cured at 250 °C, thus a nano-PI (NPI) dielectric layer with thickness ~60-100 nm was formed to afford high strain limit under uniaxial stretching as well as high strain transfer coefficient to 2D layer crystal based flexible nano electronics.[114] In situ characterization methodologies under tensile strain was enabled by a low profile homemade stretcher. The experimental setup is shown in Fig. 5.2, where Cascade probe station was customized for the stretcher to fit in.

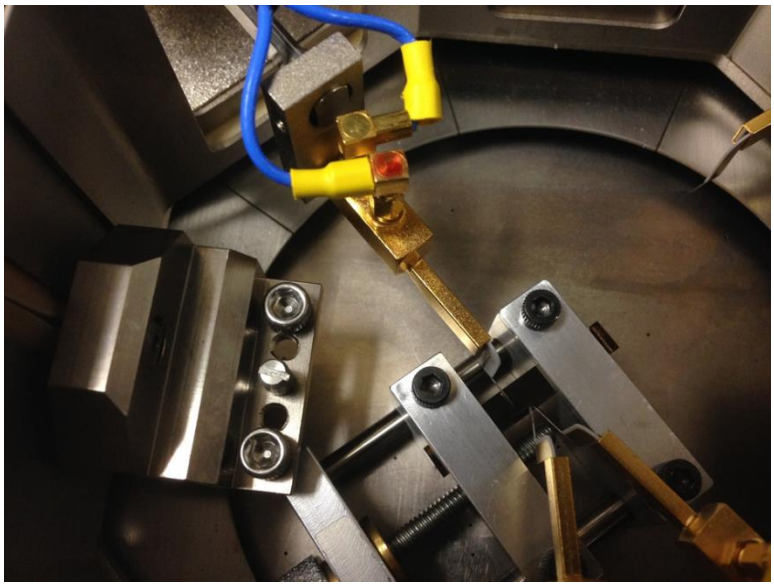

Figure 5.2: Experimental set up for in-situ electrical measurement. In this illustration, Cascade probe station was employed for electrical measurement. Polyimide substrate is under end-to-end tensile strain applied through this stretching platform.

FEW LAYER BP

We first investigated the strain tunability on crystal structure of few layer BP using this platform. Considering the unique anisotropic mechanical and electrical properties induced by the puckered honey-comb crystal structure, we carefully designed the uniaxial stretching test along both ZZ and AC directions. 532 nm polarized laser was applied in this experiments with polarization along the strain loading direction. As previously discussed that Raman spectroscopy can be generally used to determine the crystal orientation of BP according to the intensity ratio among its three finger-print peaks, therefore, the Raman spectrum can be used as both indication of the crystal orientation as well as the gauge of local strain loading.[111]

Anisotropic Raman peak shift under tensile strain

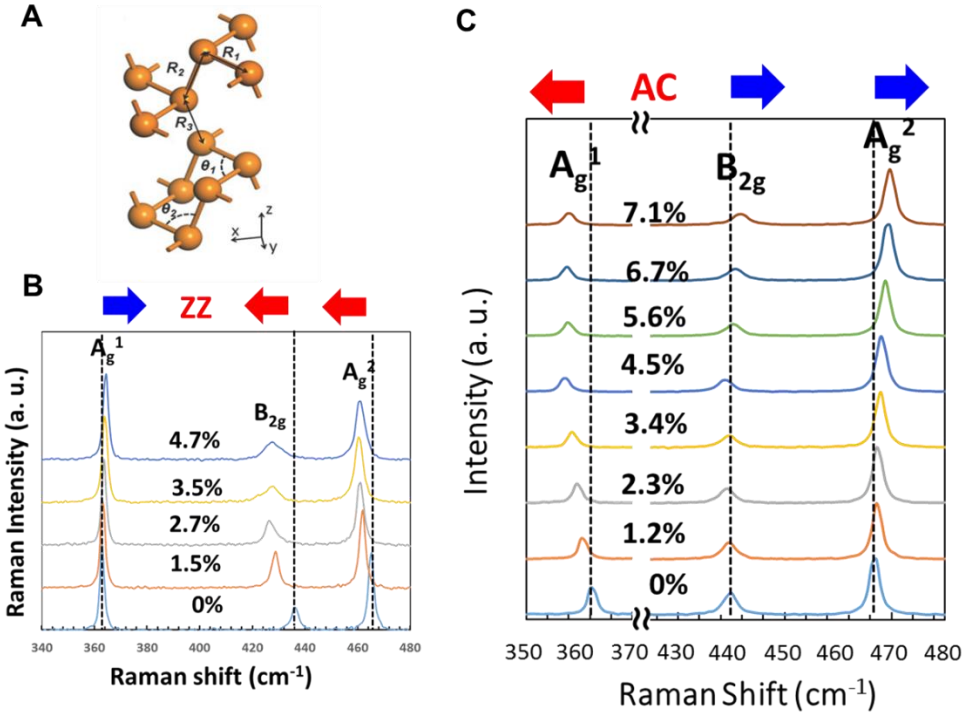

Figure 5.3: (A) Illustration of BP crystal lattice.[115] (B) Raman spectroscopy of few layer BP measured under tensile strain up to 4.7%. Strain was applied along Arm-chair direction, which was verified from the intensity ratio among A_g^1, A_g^2 and B_{2g} Raman modes. (C) Raman spectroscopy of few layer BP measured under tensile strain up to 7.1%. Strain was applied along Zig-zag direction, which was verified from the intensity ratio among A_g^1, A_g^2 and B_{2g} Raman modes.

As seen in Figure 5.3, the Raman spectrum of few layer BP exhibit strong anisotropic behavior along ZZ and AC direction under uniaxial tensile strain. When stretched along ZZ direction, red shift was observed in the two in-plane mode positions, which indicated effective p-p bond extension induced by the ZZ direction tensile strain. The slope of peak shift was estimated to be -5.2 ± 0.2 cm^{-1}/% for B_{2g} mode and -2.2±0.2 cm^{-1}/% for A_g^2 mode, respectively. Whereas, the out-of-plane mode A_g^1 was merely affected by this in-plain tensile strain. This result agrees well with the theoretical predictions regarding to the peak shift trend, yet has quite significant difference in the slope

values. The case of uniaxial strain loading along the AC direction is more complex, as is seen in Figure 5.3 (c), that significant red shift was observed in the out-of-plane A_g^1 mode, whereas blue shift was observed in both in-plane modes. And distinguished from the ZZ case, A_g^2 mode is more sensitive to the strain applied along AC direction than the B_{2g} mode. According to the theoretical predictions, this abnormal phonon strengthen under tensile strain can be explained by the flattening of the puckered structure along the AC direction, which mainly increased the vertical p-p bond length R_2 and p-p bond angle θ_2 and slightly reduced the p-p bond angle θ_1, as labeled in Figure 5.3(A). Therefore, the in-plane B_{2g} mode is least affected among the three peaks with slight hardening observed. The out-of-plane A_g^1 mode is the most affected mode with obvious phonon softening.[111, 115] Statistics of Raman peak shift under tensile strain along both ZZ and AC directions are shown in Fig. 5.4.

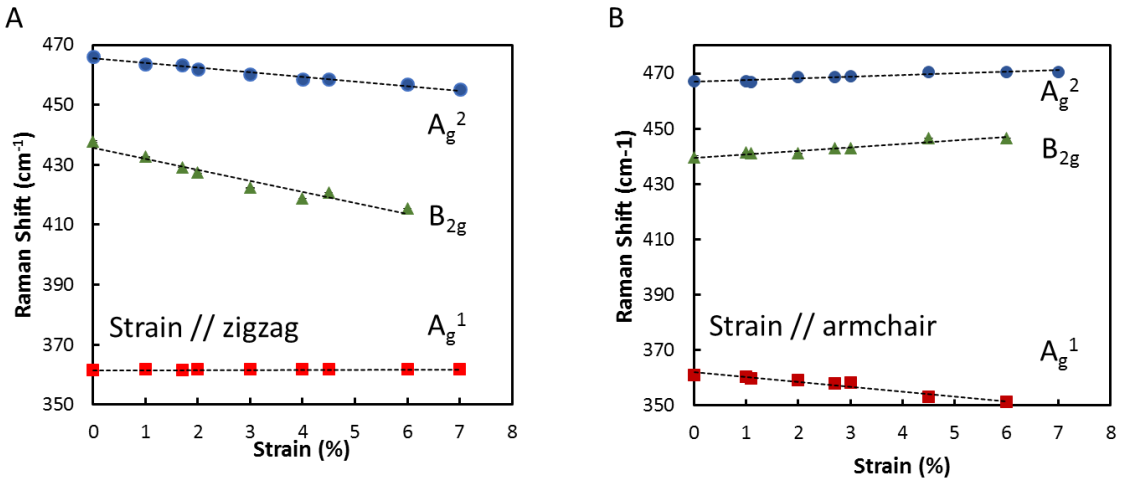

Figure 5.4: Statistics of Raman peak shift of few layer BP under tensile strain. (a) Applied strain is along zigzag direction. Red shift of A_g^2 and B_{2g} mode was observed with averaged slope ~-3.8 cm^{-1}/% and ~-1.5 cm^{-1}/% respectively. A_g1 mode exhibited negligible peak shift. (b) Applied strain is along armchair direction. Blue shift of A_g^2 and B_{2g} mode was observed with averaged slope ~ +0.6 cm^{-1}/% and ~+1.25 cm^{-1}/% respectively. A_g^1 mode exhibited red shift with averaged slope of ~-1.75 cm^{-1}/%.

Thickness dependent angle-resolved Raman

The strong anisotropic phonon behavior of few layer BP observed under tensile strain re-emphasis the importance to study the in-plane angle dependence of Raman spectroscopy of BP. Here in this work, angle-resolved Raman were conducted with an angle resolution of 15 degree. The 0 degree in this angle resolved Raman measurement was aligned along AC direction.

The anisotropic Raman response of BP is more complicated under actual measurement, where the Raman intensity is sensitive to laser wavelength, substrate insulator stack, and sample thickness. Here, 473 nm blue laser in parallel configuration, where the analyzer orientation and the plane polarized laser excitation orientation are aligned parallel to the x-axis. Different BP samples with thickness below 20nm were studied in this work since the main interest is on few layer BP. The 20 nm thick sample is treated as an bulk reference. Here, 25 nm Al_2O_3/Si substrate were adopted as the layer interference effect is negligible as the thickness of dielectric layer is much smaller than the laser wavelength (25 nm << 473 nm). The angle resolved Raman intensity for all three peaks are presented in Fig. 5. The B_{2g} mode of all three samples are showing consistent periodicity of 90 degree with the peak intensity occurring near 45 degrees. Similarly, the A_g2 mode exhibits a dumbbell shape for all three thickness with periodicity of 180 degrees and the peak intensity occurred at 0 degree. The A_g1 mode, which corresponds to out-of-plane atom oscillation, exhibit strong thickness dependence. The clearly demonstrated

dumbbell shape with periodicity of 180 degree was only observed in the thick sample, namely the bulk range. In sample with thickness below 5 nm, the polar plot of angle resolved Raman intensity loses its dumbbell shape and becomes more isotropic with much reduced intensity value. This thickness dependence observed in the out-of-plane mode intensity may reveal hidden physics that await to be further studied.

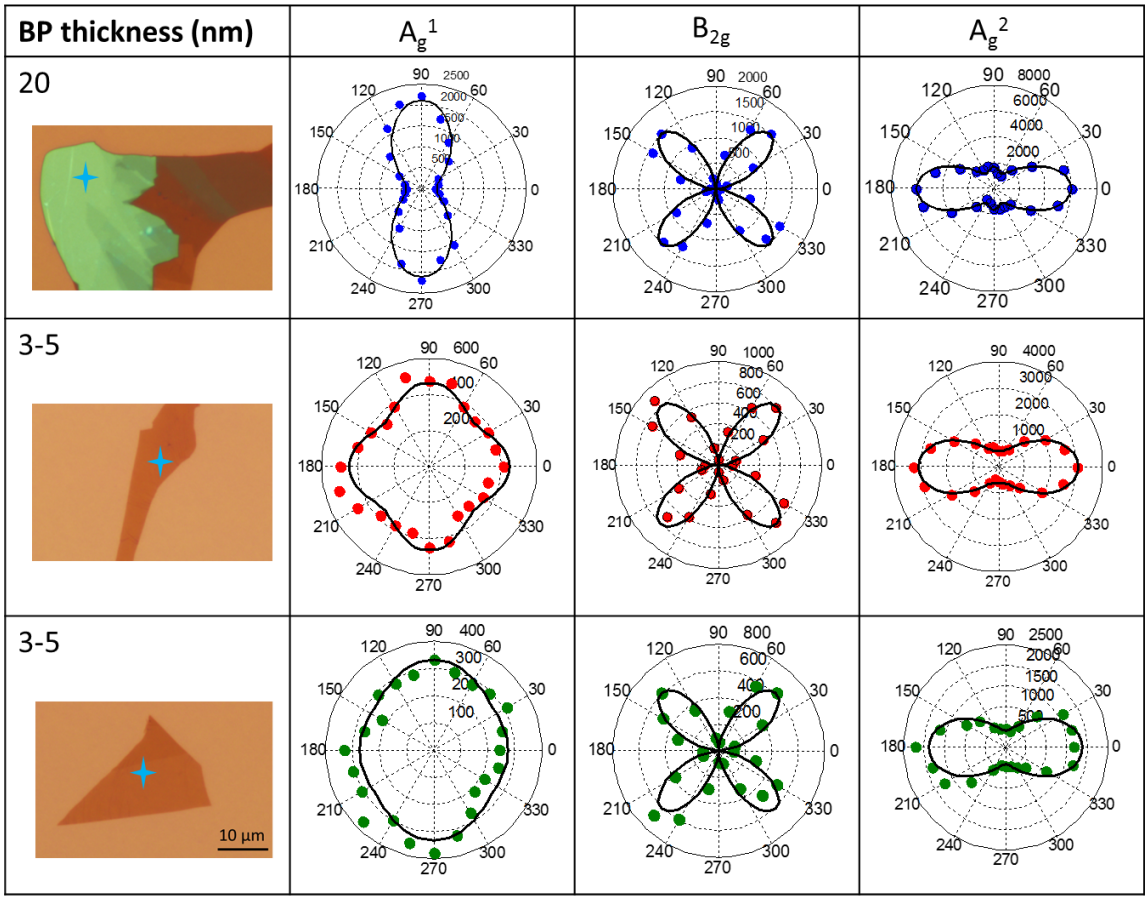

Figure 5.5: Polar plot of angle resolved Raman intensity in BP samples with different thickness. Strong thickness dependent intensity of out-of-plane mode was observed, revealing interesting physics to be further discussed. Dots are experimental data and black lines are the model fitting.

Thickness dependent intensity evolvement under strain

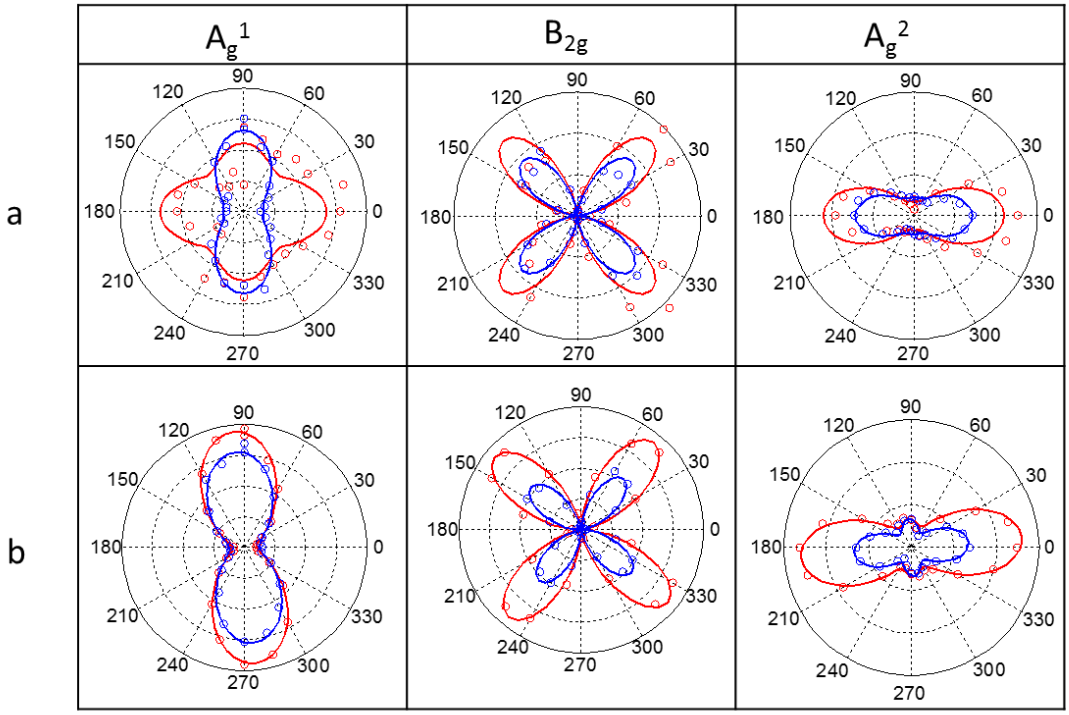

Figure 5.6: Polar plot of angle resolved Raman intensity in BP samples under tensile strain along zigzag direction. (a) Thickness is <10 nm. (b) Thickness is ~20 nm. Red line and dots are the data collected for relaxed sample under 0% of stain. Blue line and dots are the date collected for sample under 1.7% (a) and 2% (b) tensile strain, respectively. Dots are experimental data and lines are model fitting results.

Angle-resolved Raman measurement was conducted in situ under uniaxial tensile strain along either AC or ZZ directions. Thickness sensitive peak intensity evolvement has been observed when strain is applied. Shown in Fig. 5.6, the strain is along ZZ direction. Here, two sample with distinct thickness was investigated, the thicker one among which is used as the bulk reference. Examining the intensity plot of A_g^1 in Fig. 5.6 (a), interesting Raman response was observed with the reoccurrence of dumbbell shape (bulk behavior) when 1.7% of tensile strain (blue line) applied onto the thin BP sample. In contrast with

the thicker sample shown in Fig. 5.6(b), where this strain didn't change the Raman selection rules as the dumbbell shape was well preserved with only intensity reduction.

Similar effect of strain on thinner sample was observed when the uniaxial tensile strain was along the AC direction, as shown in Fig. 5.7 (a). At relatively small strain ~1%, the axis of highest intensity shifted by 90 degrees for peak A_g^1 in the thinner sample. Slightly difference in the thicker sample was observed, where the strain increased the actual Raman peak intensity of Ag1 given laser excitation angle is along AC direction.

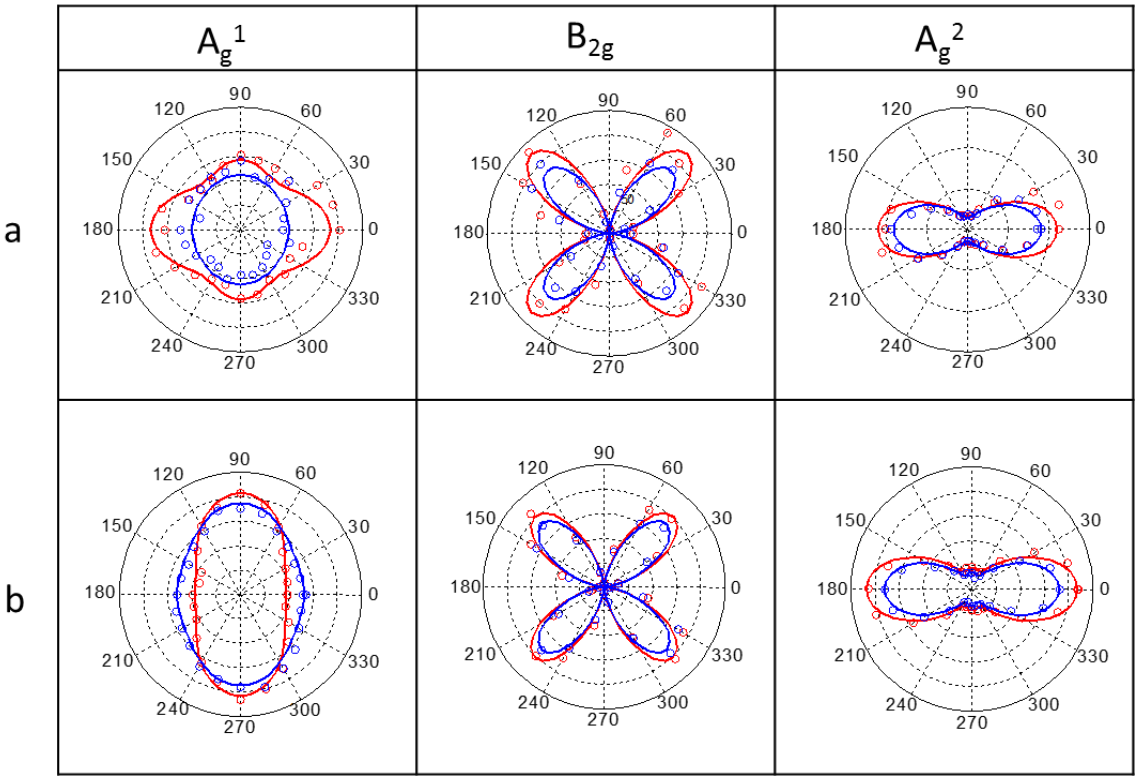

Figure 5.7: Polar plot of angle resolved Raman intensity in BP samples under tensile strain along zigzag direction. (a) Thickness is <10 nm. (b) Thickness is ~20 nm. Red line and dots are the data collected for relaxed sample under 0% of stain. Blue line and dots are the date collected for sample under 1%. Dots are experimental data and lines are model fitting results.

This strain induced Raman peak intensity evolvement was first observed and exhibited comparable trend with respect to the thickness dependence observed in relaxed BP samples. These results indicate that strain may introduce similar perturbation to the out-of-plane phonon vibrations. Unfortunately, no new symmetry was introduced under finite tensile strain in this work.

Mechanical failure

Mechanical failure was also observed in our experiments where buckle delamination of the strained BP after releasing of the tensile strain was confirmed by AFM. This result is particularly interesting for the study of mechanical adhesion between the BP few layers and PI substrate.

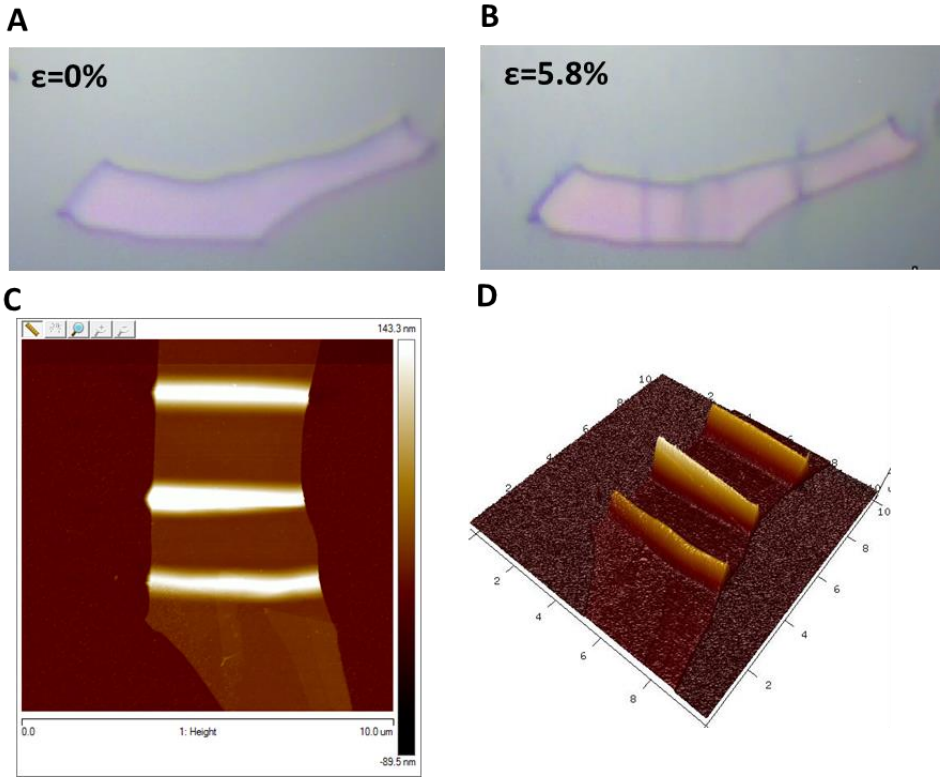

Figure 5.8: Failure mechanism of few layer BP under tensile strain. (A) optical microscopy image of BP flake with no initial strain. (B) optical microscopy image of the same BP flake under tensile strain of 5.8%. (C) Atomic force microscopic (AFM) image of the same BP flake showing buckle delamination. (D) 3D AFM image of the same BP flake.

Cracks were also observed from BP samples that went through in situ Raman measurements under tensile strain, as shown in Fig. 5.9. What worth noted is that in addition to the vertical parallel cracks induced by the horizontal tensile strain, group of parallel cracks with a particular angle to the strain direction were observed near the laser spot where BP samples were damaged from the poor thermal dissipation of PI substrate. Those cracks are the deepest according to the AFM measurement shown in Fig. 5.9.

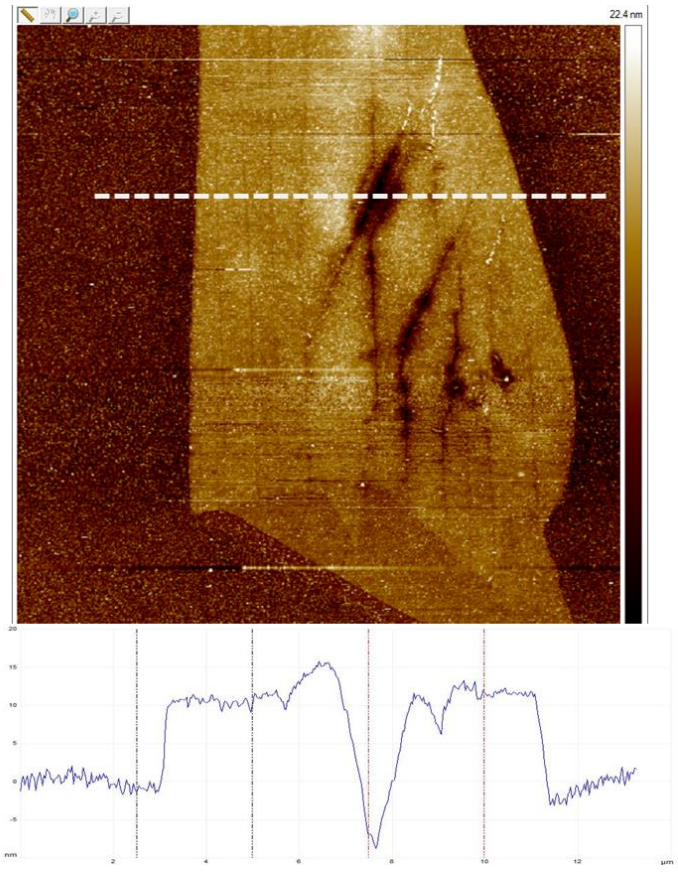

Figure 5.9: AFM image of the BP flake under tensile strain showing cracks after in situ Raman measurements. Sample thickness is 10 nm.

CVD MONOLAYER MoS_2

To verify the compatibility of this platform with various 2D layered semiconductors, monolayer chemical vapor deposition (CVD) grown MoS_2 were studied for its strain tenability on both phonon vibration modes and optical band gap.[108, 109, 112]

Raman spectroscopy

CVD grown MoS_2 was transferred onto the same thin PI substrate, as shown in Figure 5.10 (A). To study both monolayer and bilayer MoS_2 at the same time, we chose the isolated flake with nice shape and uniform add layer. The Raman spectrum of both monolayer and bilayer BP showed consistent red shift of the E_{2g} peak under tensile strain up to 3.2%, while A_{1g} peak remained stable. This result agrees well with the theoretical predictions and previously reported experimental observations.[109, 112, 116, 117] The slope of $E_{2g}{}^1$ peak shift were estimated ~3.1 cm^{-1}/% strain and 3 cm^{-1}/% strain for monolayer and bilayer, respectively. At 3.2% of strain loading, no further peak shift was observed for bilayer BP which indicate possible slippage between the add layer and beneath monolayer.

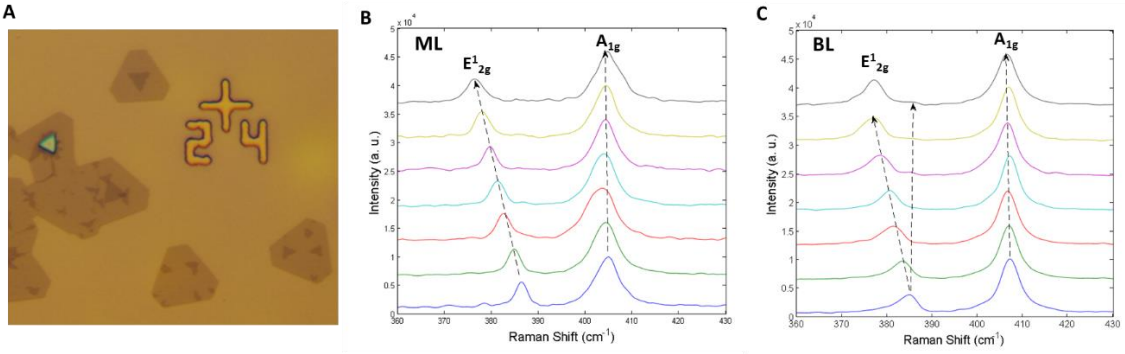

Figure 5.10: Raman spectroscopy of CVD MoS_2 under tensile strain. Both monolayer and bilayer MoS_2 was studied for the strain tenability.

Optical band gap tuning by Photoluminescence (PL)

Here, we investigate the influence of uniaxial tensile strain on the band gaps of monolayer MoS_2.[108, 109, 112] In this presented result shown in Figure 5.11, uniaxial tensile strain was applied up to 3.2%. With increasing strain, a linear redshift of 27-44 meV/% strain of the position of the A peak in photoluminescence for monolayer MoS_2 indicates a corresponding reduction in band gap energy of the material. In addition, we observed a pronounced strain-induced decrease in intensity of the photoluminescence of monolayer MoS_2. Seeing from our experimental observations, the tensile strain can strongly perturb the band structure of mono layer MoS_2 resulting in reducing band gap energy as well as the direct-to-indirect band gap switch. The strain loading was limited around 3 to 4%, which is much lower than the tensile strain loading of exfoliated BP, despite that the same substrate was employed. We attribute this reduced strain load to the possible poorer interface adhesion between CVD MoS_2 and PI substrate since wet transfer may introduce residual water molecules even after drying in N_2 environment for 24 hours. Possible solutions to increase the strain loading limit are currently under develop and will be one main direction of this project, including thermal annealing after transfer, and applying polymer nano scale adhesion layer such as self-assembled monolayers (SAM)[118] and polydopamine (PDA) layer.[119]

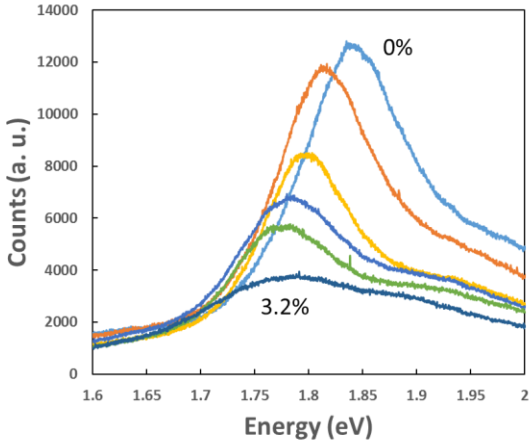

Figure 5.11: Photoluminescence of CVD monolayer MoS_2 under tensile strain up to 3.2%.

CONCLUSION

Here in this chapter, polymer based highly stretchable substrate were developed for in situ characterizations of 2D semiconductors under tensile strain, with emphasis on phonon response and band gap tuning. This platform is of potential for future in situ electrical characterization of 2D semiconductors under tensile strain, such as semiconducting to metallic phase change of CVD monolayer MoS_2.

Interesting thickness dependent Raman intensity evolvement were observed for the first time in the in-situ angle-resolved Raman measurements of few layer BP under tensile strain. Band gap closing were validated in the in-situ PL measurement of strained CVD monolayer MoS_2. The mechanical failure analysis also provided novel information about the mechanical robustness of 2D semiconductors to the community.

Chapter 6: Conclusion and Future Directions

CONCLUSION

In this dissertation, we report on our research to advance the understanding and development of two-dimensional semiconductors for high performance robust flexible nano electronics and smart nano systems. The main driving force behind this worldwide interest in flexible smart systems is the concept of Internet of Things (IoT), where the world is digitalized via connecting billions of smart devices. Specifically, for the applications in body area network, smart nano systems that are flexible, foldable and portable are of greatest need. 2D semiconductors with ultimate thickness scalability, superior mechanical robustness, and abundant material selections have become the most promising candidates for such applications. As discussed in chapter 1, in this work, we mostly focused on few layer BP for compelling performance including high mobility, high on/off ratio and tunable direct band gap ranging from 0.3 eV to 2 eV.

In chapter 2, we analyzed in detail the ambient degradation of few layer black phosphorus (BP) and the development of effective dielectric encapsulation methodology for enhancing the air stability.

In the study of few layer BP based flexible TFTs for based band applicaitons, we presented the first few layer BP based flexible thin-film transistors showing high carrier mobility, high on/off ratio, ambipolar transport with negligible hysteresis. Circuit units realized from single and double BP TFTs were reported including ambipolar inverter, small signal amplifier with voltage gain ~8.7, and frequency doubler operated at 128kHz. In addition, strong mechanical robustness was validated for the fully functional BP amplitude modulated AM demodulator, where the single BP TFT remained fully functioning with negligible degradation after 5000 cycles of bending at 1.5% of tensile strian.

In the study of 2D semiconductors for radio frequency flextronics applications, we reported the first few layer BP flexible radio frequency (RF) transistor with cut-off frequency ~20 GHz, which successfully expanded the application scenario of 2D RF devices.

In the final chapter, a polymer low-k dielectric based highly stretchable substrate was developed for investigating the strain tunabilities of 2D semiconductors. For few layer BP, thickness dependence in the angle-resolved Raman intensity evolvement under tensile strain was reported the first time. This platform is compatible with most of 2D layered van der Waals materials for in situ studies of their crystal structure, mechanical, and electrical properties.

FUTURE DIRECTIONS

As a promising candidate in 2D family with compelling performance including fast carrier transport, tunable direct band gap, and strong in-plane anisotropy, etc., the potential of this material has not been fully exploit. Therefore, in this dissertation, we proposed two directions for the future research.

The first promising research direction we proposed following the previous work is to further explore the RF applications of BP based flexible devices, for example, i) advanced 2D dielectric such as few layer h-BN can be adopted to further increase the operation frequency, and ii) integration of multiple devices for large scale circuit and fully functional system applications.

The second direction for future research is to focus more on the study of ultra-thin phosphorene such as monolayer and bilayer. For example, the possible change in symmetry due to strain induced perturbation to the ultra-thin layers, which haven't been reported experimentally for far.

In general, the study of 2D semiconductors for flexible smart systems remains a rather inspiring and high impact field for future research and development effort.

Appendix

APPENDIX A. ANALYSIS OF BLACK PHOSPHORUS FREQUENCY MULTIPLIER

Flexible BP transistor is biased near the minimum conduction point V_{min} where the drain current I_d is in the sub-threshold region and can be functionally modeled as the sum of the sub-threshold hole and electron current given by Equation A1,where I_o depends upon fixed parameters including transistor device geometry, mobility, drain bias and threshold voltage. [S120]

$$I_d \approx I_o \exp(-\beta V_g) + I_o \exp(\beta V_g), \tag{A1}$$

β is a composite parameter comprising the field-effect capacitive coupling and the thermal energy (~ 0.026eV at room temperature). V_g is the gate bias. Condensing Equation A1 leads to

$$I_d \approx 2I_o \cosh(\beta V_g), \tag{A2}$$

which can be approximated via Taylor's series approximation producing only even terms due to the even symmetry for ideal ambipolar curve.

$$I_d \approx 2I_o[1 + \frac{(\beta V_g)^2}{2!} + \frac{(\beta V_g)^4}{4!} + \cdots + \frac{(\beta V_g)^N}{N!}], \tag{A3}$$

It follows that the 2nd-order (i.e., square-law) behavior is,

$$I_d \approx 2I_o[1 + \frac{\beta^2 {V_g}^2}{2}], \tag{A4}$$

The drain output voltage of BP transistor is given by Equation A5,

$$V_d = V_{DD} - I_d R_L, \tag{A5}$$

Substituting Equation S4 into S5 yields,

$$V_d \approx V_{DD} - 2I_o R_L[1 + \frac{\beta^2 {V_g}^2}{2}], \tag{A6}$$

For frequency multipliers, the transistor gate terminal is driven by a sinusoidal input given by Equation A7.

$$V_g = V_i \cos(\omega_{in} t), \tag{A7}$$

where V_i is the input voltage amplitude, and ω_{in} is input voltage angle frequency. Substituting $V_g$into Equation A6 we obtain an expression for the drain output voltage for ambipolar FET.

$$V_d \approx V_{DD} - 2I_oR_L[1 + \frac{\beta^2 V_i^2 \cos^2(\omega_{in}t)}{2}], \quad \text{(A8)}$$

Expanding Equation S8,

$$V_d \approx V_{DD} - 2I_oR_L[1 + \frac{\beta^2 V_i^2}{4} + \frac{\beta^2 V_i^2}{4}\cos(2\omega_{in}t)], \quad \text{(A9)}$$

Therefore, the AC coupled output of an ideal ambipolar transistor frequency multiplier is given by Equation A10 to 2nd-order. It is evident that the output frequency is double the input frequency and the output amplitude scales as the square of the input amplitude.

$$V_{out} \approx \frac{I_oR_L\beta^2}{2} V_i^2\cos(2\omega_{in}t), \quad \text{(A10)}$$

We note that asymmetry in the ambipolar curve will lead to odd harmonics at the output including the fundamental input frequency.

APPENDIX B. ANALYSIS OF BLACK PHOSPHORUS AM DEMODULATOR

We designed and fabricated flexible BP transistor based amplitude modulated (AM) demodulator and biased the BP transistor near its minimum conduction point, as analyzed in the frequency multiplier. Equation B1 presents the case for an AM input signal,

$$V_{in} = (1 + mcos(\omega_m t))V_i cos(\omega_c t), \quad \text{(B1)}$$

where ω_m represents the frequency of the modulated signal, ω_c is the carrier frequency, V_i is the amplitude of the carrier and m is the modulation index. Substituting Equation B1 in Equation A6, the FET drain output is given as

$$V_D \approx V_{DD} - 2I_oR_L[1 + \frac{\beta^2[(1+mcos(\omega_m t))V_i cos(\omega_c t)]^2}{2}], \quad \text{(B2)}$$

Expanding the output equation yields

$$V_D \approx V_{DD} - 2I_oR_L - I_oR_L\beta^2\left(\frac{V_i^2}{2}+\frac{mV_i^2}{4}\right) - I_oR_L\beta^2[mV_i^2 cos\omega_m t + \frac{mV_i^2}{4}cos2\omega_m t + \left(\frac{V_i^2}{2}+\frac{mV_i^2}{4}\right) cos2\omega_c + \frac{mV_i^2}{2}cos(2\omega_c+\omega_m)t) + \frac{mV_i^2}{2}cos(2\omega_c-\omega_m)t) + \frac{m^2V_i^2}{8}cos\big((2\omega_c+2\omega_m)t\big) + \frac{m^2V_i^2}{8}cos\big((2\omega_c-2\omega_m)t\big)], \quad \text{(B3)}$$

where the equation contains the demodulated output signal V_{out} at frequency ω_m, higher order harmonics and intermodulation terms, and a DC component. The demodulated baseband output V_{out} can be isolated as

$$V_{out} \approx I_oR_Lm\beta^2V_i^2cos(\omega_m t), \quad \text{(B4)}$$

From this analysis, it is evident that the output voltage V_{out} is linearly dependent on the modulation index *m,* and is quadratically dependent on the amplitude V_i. We note that asymmetry in the ambipolar curve will lead to odd harmonics at the output including the carrier feed-through.

APPENDIX C. FABRICATION PROCESS

C1. Preparation of flexible substrate

1 DuPont™ Kapton® polyimide film
- 50 HN and 100 HN for highly stretchable devices
- 300 HN and 500 HN for back-gated devices
- 500 HN for top-gated (RF) devices

2 Acetone rinse + Isopropyl Alcohol (IPA) rinse + blow dry with N_2

3 Attach polyimide film onto carrier Si wafers

4 Spin-coat liquid polyimide (PI-2547) (2-step coating)
- Ramp up to 500 rpm @ 100 rpm/s, 5 seconds
- Ramp up to 3000 rpm @ 100 rpm/s, 30 seconds

5 Cure polyimide substrate in N_2 (Whipmix pro oven- recipe #8N)

- Ramp up to 200 °C @ rate of 4°C/min, hold for 30 mins.
- Ramp up to 300 °C @ rate of 2.5°C/min, hold for 48 mins.
- Cool down to 50 °C.

6 Repeat step 3-5 for the other side of polyimide substrate to obtain double side curing.

C2. Flexible BP Transistors with Back Gate

1 Double side cured PI substrate. (300 HN or 500 HN)

2 Acetone rinse + IPA rinse + N_2 gun blowing dry.

3 Back gate

- Deposit Ti/Pd=2 nm / 50 nm via electron beam evaporation

4 Back gate dielectric

- Deposit Al_2O_3 = 25 nm via atomic layer deposition (ALD) @ 250°C

5 E-beam alignment mark

- Acetone rinse + IPA rinse + N_2 gun blowing dry.
- Spin-coat photoresist AZ5209
    - Ramp up to 500 rpm @ 100 rpm/s, 5 seconds
    - Ramp up to 4000 rpm @ 2000 rpm/s, 30 seconds
- Bake at 90 °C for 2 mins
- Patterned by photo lithography.
- Develop in photoresist developer for 1 min.
- DI water rinse + N_2 blowing dry
- Metal deposition via e-beam evaporation (Ti/Au= 3nm/50 nm)

- lift off in acetone (RT overnight or heated up to 65°C for 20 mins) + IPA rinse + N_2 blowing dry

6 Few layer black phosphorus exfoliation

7 Source and drain electrode

- Spin-coat Polymethyl methacrylate (PMMA) A4 (4000 rpm for 40 sec)
- Bake at 180 °C for 2 mins
- Spin-coat E-spacer (4000 rpm for 40 sec)
- Pattern via e-beam lithography
- Develop in MIBK:IPA=1:3 for 2 mins
- IPA rinse
- Deposit contact metal via e-beam evaporation (Ti/Au = 2 nm/70 nm)
- Lift off in acetone (RT overnight) + acetone rinse + IPA rinse + N_2 blowing dry

8 Dielectric encapsulation

- Deposit Al_2O_3=25nm via ALD at 200 °C

9 Measurement in Cascade probe station

C3. Flexible BP Transistors with Top Gate

1 Double side cured PI substrate. (500 HN)

2 Acetone rinse + IPA rinse + N_2 gun blowing dry.

3 Dielectric adhesion layer

- Deposit Al_2O_3 = 25 nm via atomic layer deposition (ALD) @ 250°C

4 E-beam alignment mark

- Acetone rinse + IPA rinse + N_2 gun blowing dry.

- Spin-coat photoresist AZ5209
    - Ramp up to 500 rpm @ 100 rpm/s, 5 seconds
    - Ramp up to 4000 rpm @ 2000 rpm/s, 30 seconds
- Bake at 90 °C for 2 mins
- Patterned by photo lithography.
- Develop in photoresist developer for 1 min.
- DI water rinse + N_2 blowing dry
- Metal deposition via e-beam evaporation (Ti/Au= 3nm/50 nm)
- lift off in acetone (RT overnight or heated up to 65°C for 20 mins) + IPA rinse + N_2 blowing dry

5 Few layer black phosphorus exfoliation

6 Source and drain electrode

- Spin-coat PMMA EL6 (4000 rpm for 40 sec)
- Bake at 180 °C for 2 mins
- Spin-coat PMMA A4 (4000 rpm for 40 sec)
- Bake at 180 °C for 2 mins
- Spin-coat E-spacer (4000 rpm for 40 sec)
- Pattern via e-beam lithography
- Develop in MIBK:IPA=1:3 for 2 mins
- IPA rinse
- Deposit contact metal via e-beam evaporation (Ti/Au = 2 nm/50 nm)
- Lift off in acetone (RT overnight) + acetone rinse + IPA rinse + N_2 blowing dry

7 Top gate dielectric

- Deposit Al_2O_3=25nm via ALD at 200 °C

8 Top gate electrode

- Spin-coat PMMA EL6 (4000 rpm for 40 sec)
- Bake at 180 °C for 2 mins
- Spin-coat PMMA A4 (4000 rpm for 40 sec)
- Bake at 180 °C for 2 mins
- Spin-coat E-spacer (4000 rpm for 40 sec)
- Pattern via e-beam lithography
- Develop in MIBK:IPA=1:3 for 2 mins
- IPA rinse
- Deposit contact metal via e-beam evaporation (Ti/Au = 2 nm/50 nm)
- Lift off in acetone (RT overnight) + acetone rinse + IPA rinse + N_2 blowing dry

9 Measurement in Cascade probe station

C4. BP Under Tensile Strain

1 Double side cured PI substrate. (50 HN or 100 HN)

2 Acetone rinse + IPA rinse + N_2 gun blowing dry.

3 Bottom metal layer

- Deposit Cr/Pd=3 nm / 50 nm via electron beam evaporation

4 Spin-coat diluted liquid polyimide (NPI) (2-step coating)

- Ramp up to 500 rpm @ 100 rpm/s, 5 seconds
- Ramp up to 6000 rpm @ 1000 rpm/s, 30 seconds

5 Cure polyimide substrate in N_2 (Whipmix pro oven- recipe #8N)

- Ramp up to 200 °C @ rate of 4°C/min, hold for 30 mins.
- Ramp up to 300 °C @ rate of 2.5°C/min, hold for 48 mins.

- Cool down to 50 °C.

6 E-beam alignment mark

- Acetone rinse + IPA rinse + N_2 gun blowing dry.
- Spin-coat photoresist AZ5209
    - Ramp up to 500 rpm @ 100 rpm/s, 5 seconds
    - Ramp up to 4000 rpm @ 2000 rpm/s, 30 seconds
- Bake at 90 °C for 2 mins
- Patterned by photo lithography.
- Develop in photoresist developer for 1 min.
- DI water rinse + N_2 blowing dry
- Metal deposition via e-beam evaporation (Ti/Au= 3nm/50 nm)
- lift off in acetone (RT overnight or heated up to 65°C for 20 mins) + IPA rinse + N_2 blowing dry

7 Few layer black phosphorus exfoliation

8
- Spin-coat PMMA A4 (4000 rpm for 40 sec)
- Bake at 180 °C for 2 mins

9 Raman and PL measurement

C5. CVD Monolayer MoS_2 Wet Transfer

1 Acetone rinse + IPA rinse + N_2 gun blowing dry.

3
- Spin-coat PMMA A4 (4000 rpm for 40 sec)
- Bake at 180 °C for 2 mins

4 Repeat step 3 for 10 times

5 Wet etching of SiO_2 substrate in buffer oxide etchant (BOE)

- Soak overnight at room temperature

6 - Fishing PMMA/MoS_2 stack in BOE using Si wafer
- Rinse in still water
- Fishing out using target substrate

7 Air dry for 24 hours

8 Bake at 100 °C for 10 mins

9 Acetone soaking overnight

10 Acetone rinse + IPA rinse + N_2 gun blowing dry.

11 - Spin-coat PMMA A4 (4000 rpm for 40 sec)
- Bake at 180 °C for 2 mins

References

1. Novoselov, K. S.; Geim, A. K.; Morozov, S. V.; Jiang, D.; Katsnelson, M. I.; Grigorieva, I. V.; Dubonos, S. V.; Firsov, A. A. *Nature* **2005,** 438, (7065), 197-200.
2. Geim, A. K.; Novoselov, K. S. *Nat Mater* **2007,** 6, (3), 183-191.
3. Schwierz, F. *Nat Nano* **2010,** 5, (7), 487-496.
4. Moon, J. S.; Seo, H. C.; Son, K. A.; Yang, B.; Le, D.; Fung, H.; Schmitz, A. In *Zero-bias THz detection using graphene transistors*, Microwave Symposium (IMS), 2015 IEEE MTT-S International, 17-22 May 2015, 2015; pp 1-4.
5. Yeh, C.-H.; Lain, Y.-W.; Chiu, Y.-C.; Liao, C.-H.; Moyano, D. R.; Hsu, S. S. H.; Chiu, P.-W. *ACS Nano* **2014,** 8, (8), 7663-7670.
6. Petrone, N.; Meric, I.; Chari, T.; Shepard, K. L.; Hone, J. *Electron Devices Society, IEEE Journal of the* **2015,** 3, (1), 44-48.
7. Kim, S.; Konar, A.; Hwang, W. S.; Lee, J. H.; Lee, J.; Yang, J.; Jung, C.; Kim, H.; Yoo, J. B.; Choi, J. Y.; Jin, Y. W.; Lee, S. Y.; Jena, D.; Choi, W.; Kim, K. *Nat Commun* **2012,** 3, 1011.
8. Wang, Q. H.; Kalantar-Zadeh, K.; Kis, A.; Coleman, J. N.; Strano, M. S. *Nat Nanotechnol* **2012,** 7, (11), 699-712.
9. Jin, Z. H.; Li, X. D.; Mullen, J. T.; Kim, K. W. *Physical Review B* **2014,** 90, (4), 045422.
10. Wang, C.; Chien, J.-C.; Fang, H.; Takei, K.; Nah, J.; Plis, E.; Krishna, S.; Niknejad, A. M.; Javey, A. *Nano Letters* **2012,** 12, (8), 4140-4145.
11. Krasnozhon, D.; Lembke, D.; Nyffeler, C.; Leblebici, Y.; Kis, A. *Nano Letters* **2014,** 14, (10), 5905-5911.
12. Sanne, A.; Ghosh, R.; Rai, A.; Yogeesh, M. N.; Shin, S. H.; Sharma, A.; Jarvis, K.; Mathew, L.; Rao, R.; Akinwande, D.; Banerjee, S. *Nano Letters* **2015,** 15, (8), 5039-5045.
13. Fei, R.; Yang, L. *Nano Lett* **2014,** 14, (5), 2884-9.
14. Xia, F.; Wang, H.; Jia, Y. *Nat Commun* **2014,** 5, 4458.
15. Li, L.; Yu, Y.; Ye, G. J.; Ge, Q.; Ou, X.; Wu, H.; Feng, D.; Chen, X. H.; Zhang, Y. *Nature nanotechnology* **2014,** 9, (5), 372-7.
16. Zhang, S.; Yang, J.; Xu, R.; Wang, F.; Li, W.; Ghufran, M.; Zhang, Y. W.; Yu, Z.; Zhang, G.; Qin, Q.; Lu, Y. *ACS Nano* **2014,** 8, (9), 9590-6.
17. Wei, Q.; Peng, X. *Applied Physics Letters* **2014,** 104, (25), 251915.
18. Qiao, J.; Kong, X.; Hu, Z. X.; Yang, F.; Ji, W. *Nat Commun* **2014,** 5, 4475.
19. Castellanos-Gomez, A.; Vicarelli, L.; Prada, E.; Island, J. O.; Narasimha-Acharya, K. L.; Blanter, S. I.; Groenendijk, D. J.; Buscema, M.; Steele, G. A.; Alvarez, J. V.; Zandbergen, H. W.; Palacios, J. J.; van der Zant, H. S. J. *2D Materials* **2014,** 1, (2), 025001.
20. Morita, A.; Sasaki, T. *Journal of the Physical Society of Japan* **1989,** 58, (5), 1694-1704.
21. Tauc, J. *Materials Research Bulletin* **1968,** 3, (1), 37-46.
22. Wood, J. D.; Wells, S. A.; Jariwala, D.; Chen, K. S.; Cho, E.; Sangwan, V. K.; Liu, X.; Lauhon, L. J.; Marks, T. J.; Hersam, M. C. *Nano Lett* **2014**.

23. Kim, J.-S.; Liu, Y.; Zhu, W.; Kim, S.; Wu, D.; Tao, L.; Dodabalapur, A.; Lai, K.; Akinwande, D. *Sci. Rep.* **2015,** 5, 8989.
24. Zhu, W.; Park, S.; Yogeesh, M. N.; McNicholas, K. M.; Bank, S. R.; Akinwande, D. *Nano Lett* **2016,** 16, (4), 2301-6.
25. Gao, C.; Wei, T.; Duewer, F.; Lu, Y.; Xiang, X.-D. *Applied Physics Letters* **1997,** 71, (13), 1872-1874.
26. Carbonnière, P.; Pouchan, C. *Chemical Physics Letters* **2008,** 462, (4–6), 169-172.
27. Akinwande, D.; Petrone, N.; Hone, J. *Nat Commun* **2014,** 5, 5678.
28. Schwierz, F. *Proceedings of the IEEE* **2013,** 101, (7), 1567-1584.
29. Lee, J.; Ha, T. J.; Li, H.; Parrish, K. N.; Holt, M.; Dodabalapur, A.; Ruoff, R. S.; Akinwande, D. *ACS Nano* **2013,** 7, (9), 7744-50.
30. Lee, J.; Ha, T. J.; Parrish, K. N.; Chowdhury, S. F.; Tao, L.; Dodabalapur, A.; Akinwande, D. *Ieee Electron Device Letters* **2013,** 34, (2), 172-174.
31. Petrone, N.; Meric, I.; Hone, J.; Shepard, K. L. *Nano Letters* **2012**, (13), 121-125.
32. Chang, H. Y.; Yang, S.; Lee, J.; Tao, L.; Hwang, W. S.; Jena, D.; Lu, N.; Akinwande, D. *ACS Nano* **2013,** 7, (6), 5446-52.
33. Lee, G. H.; Yu, Y. J.; Cui, X.; Petrone, N.; Lee, C. H.; Choi, M. S.; Lee, D. Y.; Lee, C.; Yoo, W. J.; Watanabe, K.; Taniguchi, T.; Nuckolls, C.; Kim, P.; Hone, J. *ACS Nano* **2013,** 7, (9), 7931-6.
34. Liu, H.; Neal, A. T.; Zhu, Z.; Luo, Z.; Xu, X.; Tomanek, D.; Ye, P. D. *ACS Nano* **2014,** 8, (4), 4033-41.
35. Kobayashi, T.; Bando, M.; Kimura, N.; Shimizu, K.; Kadono, K.; Umezu, N.; Miyahara, K.; Hayazaki, S.; Nagai, S.; Mizuguchi, Y.; Murakami, Y.; Hobara, D. *Applied Physics Letters* **2013,** 102, (2), 023112-4.
36. Rahimi, S.; Tao, L.; Chowdhury, S. F.; Park, S.; Jouvray, A.; Buttress, S.; Rupesinghe, N.; Teo, K.; Akinwande, D. *ACS Nano* **2014,** 8, (10), 10471-9.
37. Bae, S.; Kim, H.; Lee, Y.; Xu, X.; Park, J. S.; Zheng, Y.; Balakrishnan, J.; Lei, T.; Kim, H. R.; Song, Y. I.; Kim, Y. J.; Kim, K. S.; Ozyilmaz, B.; Ahn, J. H.; Hong, B. H.; Iijima, S. *Nat Nanotechnol* **2010,** 5, (8), 574-8.
38. Cheng, R.; Jiang, S.; Chen, Y.; Liu, Y.; Weiss, N.; Cheng, H. C.; Wu, H.; Huang, Y.; Duan, X. *Nat Commun* **2014,** 5, 5143.
39. Ma, N.; Jena, D. *Physical Review X* **2014,** 4, (1), 011043.
40. Das, S.; Gulotty, R.; Sumant, A. V.; Roelofs, A. *Nano Lett* **2014,** 14, (5), 2861-6.
41. Mitzi, D. B.; Kosbar, L. L.; Murray, C. E.; Copel, M.; Afzali, A. *Nature* **2004,** 428, (6980), 299-303.
42. Wei, C.-Y.; Shu-Hao, K.; Yu-Ming, H.; Wen-Chieh, H.; Adriyanto, F.; Yeong-Her, W. *Electron Device Letters, IEEE* **2011,** 32, (1), 90-92.
43. Hsu, H.-H.; Chang, C.-Y.; Cheng, C.-H. *IEEE Electron Device Letters* **2013,** 34, (6), 768-770.
44. Nathan, A.; Ahnood, A.; Cole, M. T.; Lee, S.; Suzuki, Y.; Hiralal, P.; Bonaccorso, F.; Hasan, T.; Garcia-Gancedo, L.; Dyadyusha, A.; Haque, S.; Andrew, P.; Hofmann, S.; Moultrie, J.; Chu, D. P.; Flewitt, A. J.; Ferrari, A. C.; Kelly, M. J.; Robertson, J.;

Amaratunga, G. A. J.; Milne, W. I. *Proceedings of the Ieee* **2012,** 100, (Special Centennial Issue), 1486-1517.
45. Hsu, H.-H.; Chang, C.-Y.; Cheng, C.-H. *Electron Device Letters, IEEE* **2013,** 34, (6), 768-770.
46. Li, Y. V.; Ramirez, J. I.; Sun, K. G.; Jackson, T. N. *Electron Device Letters, IEEE* **2013,** 34, (7), 891-893.
47. Morita, A. *Applied Physics A* **1986,** 39, (4), 227-242.
48. Buscema, M.; Groenendijk, D. J.; Blanter, S. I.; Steele, G. A.; van der Zant, H. S. J.; Castellanos-Gomez, A. *Nano Letters* **2014,** 14, (6), 3347-3352.
49. Buscema, M.; Groenendijk, D. J.; Steele, G. A.; van der Zant, H. S. J.; Castellanos-Gomez, A. *Nat Commun* **2014,** 5.
50. Deng, Y.; Luo, Z.; Conrad, N. J.; Liu, H.; Gong, Y.; Najmaei, S.; Ajayan, P. M.; Lou, J.; Xu, X.; Ye, P. D. *ACS Nano* **2014,** 8, (8), 8292-8299.
51. Engel, M.; Steiner, M.; Avouris, P. *Nano Letters* **2014,** 14, (11), 6414-6417.
52. Hong, T.; Chamlagain, B.; Lin, W.; Chuang, H.-J.; Pan, M.; Zhou, Z.; Xu, Y.-Q. *Nanoscale* **2014,** 6, (15), 8978-8983.
53. Tran, V.; Soklaski, R.; Liang, Y. F.; Yang, L. *Physical Review B* **2014,** 89, (23), 235319.
54. Nayfeh, O. M. *Electron Device Letters, IEEE* **2011,** 32, (10), 1349-1351.
55. Yeh, C. H.; Lain, Y. W.; Chiu, Y. C.; Liao, C. H.; Moyano, D. R.; Hsu, S. S.; Chiu, P. W. *ACS Nano* **2014,** 8, (8), 7663-70.
56. Wood, J. D.; Wells, S. A.; Jariwala, D.; Chen, K. S.; Cho, E.; Sangwan, V. K.; Liu, X.; Lauhon, L. J.; Marks, T. J.; Hersam, M. C. *Nano Lett* **2014,** 14, (12), 6964-70.
57. Kim, J.-S.; Liu, Y.; Zhu, W.; Kim, S.; Wu, D.; Tao, L.; Dodabalapur, A.; Lai, K.; Akinwande, D. *arXiv preprint arXiv:1412.0355* **2014**.
58. Tao, L.; Lee, J.; Akinwande, D. *Journal of Vacuum Science & Technology B* **2011,** 29, (6), -.
59. Popov, I.; Seifert, G.; Tománek, D. *Physical Review Letters* **2012,** 108, (15), 156802.
60. Das, S.; Demarteau, M.; Roelofs, A. *ACS Nano* **2014,** 8, (11), 11730-8.
61. Cai, Y.; Zhang, G.; Zhang, Y. W. *Sci Rep* **2014,** 4, 6677.
62. Chang, H. Y.; Zhu, W.; Akinwande, D. *Applied Physics Letters* **2014,** 104, (11), -.
63. Du, Y.; Liu, H.; Deng, Y.; Ye, P. D. *ACS Nano* **2014,** 8, (10), 10035-42.
64. Li, S. L.; Miyazaki, H.; Kumatani, A.; Kanda, A.; Tsukagoshi, K. *Nano Lett* **2010,** 10, (7), 2357-62.
65. Guerriero, E.; Polloni, L.; Rizzi, L. G.; Bianchi, M.; Mondello, G.; Sordan, R. *Small* **2012,** 8, (3), 356-61.
66. Wang, H.; Wang, X.; Xia, F.; Wang, L.; Jiang, H.; Xia, Q.; Chin, M. L.; Dubey, M.; Han, S. J. *Nano Lett* **2014,** 14, (11), 6424-9.
67. Ramón, M. E.; Parrish, K. N.; Chowdhury, S. F.; Magnuson, C. W.; Movva, H. C. P.; Ruoff, R. S.; Banerjee, S. K.; Akinwande, D. *IEEE Transactions on Nanotechnology* **2012,** 11, (5), 877-883.

68. Han, S. J.; Jenkins, K. A.; Valdes Garcia, A.; Franklin, A. D.; Bol, A. A.; Haensch, W. *Nano Lett* **2011,** 11, (9), 3690-3.
69. Gray, P. R.; Hurst, P. J.; Meyer, R. G.; Lewis, S. H., *Analysis and design of analog integrated circuits*. John Wiley & Sons: 2008.
70. Razavi, B. *Solid-State Circuits, IEEE Journal of* **1999,** 34, (3), 268-276.
71. Parrish, K. N.; Akinwande, D. *Applied Physics Letters* **2011,** 99, (22), -.
72. Wang, H.; Nezich, D.; Kong, J.; Palacios, T. *Ieee Electron Device Letters* **2009,** 30, (5), 547-549.
73. Fan, J.; Yuen, J. D.; Wang, M.; Seifter, J.; Seo, J. H.; Mohebbi, A. R.; Zakhidov, D.; Heeger, A.; Wudl, F. *Adv Mater* **2012,** 24, (16), 2186-90.
74. Wang, H.; Hsu, A.; Ki Kang, K.; Kong, J.; Palacios, T. In *Gigahertz ambipolar frequency multiplier based on CVD graphene*, Electron Devices Meeting (IEDM), 2010 IEEE International, 6-8 Dec. 2010, 2010; pp 23.6.1-23.6.4.
75. Rutherglen, C.; Burke, P. *Nano Letters* **2007,** 7, (11), 3296-3299.
76. Zhu, W. J.; Farmer, D. B.; Jenkins, K. A.; Ek, B.; Oida, S.; Li, X. S.; Bucchignano, J.; Dawes, S.; Duch, E. A.; Avouris, P. *Applied Physics Letters* **2013,** 102, (23), 233102.
77. Elahi, M.; Khaliji, K.; Tabatabaei, S. M.; Pourfath, M.; Asgari, R. *arXiv preprint arXiv:1407.7706* **2014**.
78. Wei, Q.; Peng, X. H. *Applied Physics Letters* **2014,** 104, (25).
79. Kim, K. S.; Zhao, Y.; Jang, H.; Lee, S. Y.; Kim, J. M.; Kim, K. S.; Ahn, J. H.; Kim, P.; Choi, J. Y.; Hong, B. H. *Nature* **2009,** 457, (7230), 706-10.
80. Argon, A. S.; Bessonov, M. *Philosophical Magazine* **1977,** 35, (4), 917-933.
81. Lee, E. H. *Journal of Applied Mechanics* **1969,** 36, (1), 1-6.
82. Hook, T. B.; Ma, T. *Applied physics letters* **1986,** 48, (18), 1208-1210.
83. Zhu, W. J.; Ma, T. P.; Zafar, S.; Tamagawa, T. *Electron Device Letters, IEEE* **2002,** 23, (10), 597-599.
84. Yeh, W. K.; Wang, C. C.; Hsu, C. W.; Fang, Y. K.; Wu, S. M.; Ou, C. C.; Lin, C. L.; Gan, K. J.; Weng, C. J.; Chen, P. Y.; Jiann-Shiun, Y.; Liou, J. J. In *Impact of oxide trap charge on performance of strained fully depleted SOI metal-gate MOSFET*, Electron Devices and Solid-State Circuits, 2009. EDSSC 2009. IEEE International Conference of, 25-27 Dec. 2009, 2009; pp 197-200.
85. Klauk, H.; Halik, M.; Zschieschang, U.; Eder, F.; Rohde, D.; Schmid, G.; Dehm, C. *Electron Devices, IEEE Transactions on* **2005,** 52, (4), 618-622.
86. Wang, H.; Yu, L.; Lee, Y. H.; Shi, Y.; Hsu, A.; Chin, M. L.; Li, L. J.; Dubey, M.; Kong, J.; Palacios, T. *Nano Lett* **2012,** 12, (9), 4674-80.
87. Das, S.; Zhang, W.; Demarteau, M.; Hoffmann, A.; Dubey, M.; Roelofs, A. *Nano Letters* **2014,** 14, (10), 5733-5739.
88. Woomer, A. H.; Farnsworth, T. W.; Hu, J.; Wells, R. A.; Donley, C. L.; Warren, S. C. *arXiv preprint arXiv:1505.04663* **2015**.
89. Jena, D.; Konar, A. *Physical Review Letters* **2007,** 98, (13), 136805.
90. Zhu, W.; Yogeesh, M. N.; Yang, S.; Aldave, S. H.; Kim, J. S.; Sonde, S.; Tao, L.; Lu, N.; Akinwande, D. *Nano Lett* **2015,** 15, (3), 1883-90.

91. Wang, H.; Wang, X.; Xia, F.; Wang, L.; Jiang, H.; Xia, Q.; Chin, M. L.; Dubey, M.; Han, S.-j. *Nano Letters* **2014,** 14, (11), 6424-6429.
92. Han, L.; Neal, A. T.; Mengwei, S.; Yuchen, D.; Ye, P. D. *Electron Device Letters, IEEE* **2014,** 35, (7), 795-797.
93. Meric, I.; Han, M. Y.; Young, A. F.; Ozyilmaz, B.; Kim, P.; Shepard, K. L. *Nat Nano* **2008,** 3, (11), 654-659.
94. Parrish, K. N.; Akinwande, D. *Applied Physics Letters* **2011,** 98, (18), 183505.
95. Pierret, R. F., *Semiconductor device fundamentals*. Pearson Education India: 1996.
96. Heinze, S.; Tersoff, J.; Martel, R.; Derycke, V.; Appenzeller, J.; Avouris, P. *Physical Review Letters* **2002,** 89, (10), 106801.
97. Lam, K.-T.; Dong, Z.; Guo, J. *IEEE Electron Device Letters* **2014,** 35, (9), 963-965.
98. Sze, S. M.; Ng, K. K., *Physics of semiconductor devices*. John Wiley & Sons: 2006.
99. Shahidi, G. G.; Antoniadis, D. A.; Smith, H. I. *Electron Device Letters, IEEE* **1988,** 9, (2), 94-96.
100. Chang, H.-Y.; Yogeesh, M. N.; Ghosh, R.; Rai, A.; Sanne, A.; Yang, S.; Lu, N.; Banerjee, S. K.; Akinwande, D. *Advanced Materials* **2015**, n/a-n/a.
101. Su, L.-Y.; Huang, J. *Solid-State Electronics* **2015,** 104, 122-125.
102. Hsin-Hui, H.; Hsin-Ping, H. *Electron Device Letters, IEEE* **2015,** 36, (4), 345-347.
103. Park, S.; Chang, C. Y.; Rahimi, S.; Lee, A.; Akinwande, D. In *Flexible 2D electronics using nanoscale transparent polyimide gate dielectric*, Device Research Conference (DRC), 2015 73rd Annual, 21-24 June 2015, 2015; pp 193-194.
104. Verheyen, P.; Collaert, N.; Rooyackers, R.; Loo, R.; Shamiryan, D.; De Keersgieter, A.; Eneman, G.; Leys, F.; Dixit, A.; Goodwin, M.; Yim, Y. S.; Caymax, M.; De Meyer, K.; Absil, P.; Jurczak, M.; Biesemans, S. In *25% drive current improvement for p-type multiple gate FET (MuGFET) devices by the introduction of recessed Si_{0.8}Ge_{0.2} in the source and drain regions*, VLSI Technology, 2005. Digest of Technical Papers. 2005 Symposium on, 14-16 June 2005, 2005; pp 194-195.
105. Liow, T.-Y.; Tan, K.-M.; Lee, R. T.; Du, A.; Tung, C.-H.; Samudra, G. S.; Yoo, W.-J.; Balasubramanian, N.; Yeo, Y.-C. In *Strained n-channel FinFETs with 25 nm gate length and silicon-carbon source/drain regions for performance enhancement*, VLSI Technology, 2006. Digest of Technical Papers. 2006 Symposium on, 2006; IEEE: pp 56-57.
106. Gui, G.; Li, J.; Zhong, J. *Physical Review B* **2008,** 78, (7), 075435.
107. Lu, Y.; Guo, J. *Nano Research* **2010,** 3, (3), 189-199.
108. Nayak, A. P.; Bhattacharyya, S.; Zhu, J.; Liu, J.; Wu, X.; Pandey, T.; Jin, C.; Singh, A. K.; Akinwande, D.; Lin, J.-F. *Nat Commun* **2014,** 5.
109. Conley, H. J.; Wang, B.; Ziegler, J. I.; Haglund, R. F.; Pantelides, S. T.; Bolotin, K. I. *Nano Letters* **2013,** 13, (8), 3626-3630.
110. Peng, X.; Wei, Q.; Copple, A. *Physical Review B* **2014,** 90, (8), 085402.
111. Fei, R.; Yang, L. *Applied Physics Letters* **2014,** 105, (8), 083120.

112. Liu, Z.; Amani, M.; Najmaei, S.; Xu, Q.; Zou, X.; Zhou, W.; Yu, T.; Qiu, C.; Birdwell, A. G.; Crowne, F. J. *Nature communications* **2014,** 5.
113. Lee, J.; Chang, H.-Y.; Ha, T.-J.; Li, H.; Ruoff, R. S.; Dodabalapur, A.; Akinwande, D. In *High-performance flexible nanoelectronics: 2D atomic channel materials for low-power digital and high-frequency analog devices*, Electron Devices Meeting (IEDM), 2013 IEEE International, 9-11 Dec. 2013, 2013; pp 19.2.1-19.2.4.
114. Park, S.; Zhu, W.; Chang, H.-Y.; Yogeesh, M. N.; Ghosh, R.; Banerjee, S. K.; Akinwande, D. In *High-frequency prospects of 2D nanomaterials for flexible nanoelectronics from baseband to sub-THz devices*, 2015 IEEE International Electron Devices Meeting (IEDM), 2015; IEEE: pp 32.1. 1-32.1. 4.
115. Li, Y.; Hu, Z.; Lin, S.; Lai, S. K.; Ji, W.; Lau, S. P. *Advanced Functional Materials* **2016**, n/a-n/a.
116. Rice, C.; Young, R. J.; Zan, R.; Bangert, U.; Wolverson, D.; Georgiou, T.; Jalil, R.; Novoselov, K. S. *Physical Review B* **2013,** 87, (8), 081307.
117. McCreary, A.; Ghosh, R.; Amani, M.; Wang, J.; Duerloo, K.-A. N.; Sharma, A.; Jarvis, K.; Reed, E. J.; Dongare, A. M.; Banerjee, S. K. *ACS nano* **2016,** 10, (3), 3186-3197.
118. Wang, B.; Huang, M.; Tao, L.; Lee, S. H.; Jang, A.-R.; Li, B.-W.; Shin, H. S.; Akinwande, D.; Ruoff, R. S. *ACS nano* **2016,** 10, (1), 1404-1410.
119. Cho, J. H.; Katsumata, R.; Zhou, S. X.; Kim, C. B.; Dulaney, A. R.; Janes, D. W.; Ellison, C. J. *ACS applied materials & interfaces* **2016,** 8, (11), 7456-7463.
120. Sze, S. M.; Ng, K. K. **1981**.